

THE QUIJOTE SIMULATIONS

FRANCISCO VILLAESCUSA-NAVARRO^{1,2,†}, CHANGHOON HAHN^{3,4}, ELENA MASSARA^{1,5}, ARKA BANERJEE^{6,7,8}, ANA MARIA DELGADO^{9,1}, DOOGESH KODI RAMANAH^{10,11}, TOM CHARNOCK¹⁰, ELENA GIUSARMA^{1,12}, YIN LI^{3,4,13}, ERWAN ALLYS¹⁴, ANTOINE BROCHARD^{15,16}, CHI-TING CHIANG¹⁷, SIYU HE¹, ALICE PISANI², ANDREJ OBULJEN⁵, YU FENG^{3,4}, EMANUELE CASTORINA^{3,4}, GABRIELLA CONTARDO¹, CHRISTINA D. KREISCH², ANDRINA NICOLA², ROMAN SCOCCIMARRO¹⁸, LICIA VERDE^{19,20}, MATTEO VIEL^{21,22,23,24}, SHIRLEY HO^{1,2,25}, STEPHANE MALLAT^{26,27}, BENJAMIN WANDELT^{10,11,1}, DAVID N. SPERGEL^{2,1}

¹Center for Computational Astrophysics, Flatiron Institute, 162 5th Avenue, 10010, New York, NY, USA

²Department of Astrophysical Sciences, Princeton University, Peyton Hall, Princeton NJ 08544-0010, USA

³Department of Physics, University of California, Berkeley, CA 94720, USA

⁴Berkeley Center for Cosmological Physics, Berkeley, CA 94720, USA

⁵Waterloo Centre for Astrophysics, University of Waterloo, 200 University Ave W, Waterloo, ON N2L 3G1, Canada

⁶Kavli Institute for Particle Astrophysics and Cosmology, Stanford University, 452 LomitaMall, Stanford, CA 94305, USA

⁷Department of Physics, Stanford University, 382 Via Pueblo Mall, Stanford, CA 94305, USA

⁸SLAC National Accelerator Laboratory, 2575 Sand Hill Road, Menlo Park, CA 94025, USA

⁹Department of Physics, New York City College of Technology, Brooklyn, NY 11201, USA

¹⁰Sorbonne Universite, CNRS, UMR 7095, Institut d'Astrophysique de Paris, 98 bis boulevard Arago, 75014 Paris, France

¹¹Sorbonne Universite, Institut Lagrange de Paris, 98 bis boulevard Arago, 75014 Paris, France

¹²Department of Physics, Michigan Technological University, Houghton, MI, 49931, USA.

¹³Kavli Institute for the Physics and Mathematics of the Universe (WPI), UTIAS, The University of Tokyo, Chiba 277-8583, Japan

¹⁴Laboratoire de Physique de l'École normale supérieure, ENS, Université PSL, CNRS, Paris, France

¹⁵INRIA, ENS, PSL Research University Paris, France

¹⁶Paris Research Center, Huawei Technologies, Paris, France

¹⁷Physics Department, Brookhaven National Laboratory, Upton, NY 11973, USA

¹⁸Center for Cosmology and Particle Physics, Department of Physics, New York University, NY 10003, New York, USA

¹⁹Institut de Ciències del Cosmos, University of Barcelona, ICCUB, Barcelona 08028, Spain

²⁰Institucio Catalana de Recerca i Estudis Avancats, Passeig Lluís Companys 23, Barcelona 08010, Spain

²¹SISSA, Via Bonomea 265, 34136 Trieste, Italy

²²INFN, Sez. di Trieste, Via Valerio 2, 34127 Trieste, Italy

²³IFPU, Institute for Fundamental Physics of the Universe, via Beirut 2, 34151 Trieste, Italy

²⁴INAF, Osservatorio Astronomico di Trieste, via Tiepolo 11, I-34131 Trieste, Italy

Department of Physics, Carnegie Mellon University, Pittsburgh, PA 15213, USA

²⁶Data team, Ecole Normale Supérieure, Université PSL, 45 rue d'Ulm, 75005 Paris, France and

²⁷Collège de France, 11 place Marcelin Berthelot, 75005, Paris, France

Draft version September 13, 2019

ABSTRACT

The QUIJOTE simulations are a set of 43100 full N-body simulations spanning more than 7000 cosmological models in the $\{\Omega_m, \Omega_b, h, n_s, \sigma_8, M_\nu, w\}$ hyperplane. At a single redshift the simulations contain more than 8.5 trillions of particles over a combined volume of $43100 (h^{-1}\text{Gpc})^3$. Billions of dark matter halos and cosmic voids have been identified in the simulations, whose runs required more than 35 million core hours. The QUIJOTE simulations have been designed for two main purposes: 1) to quantify the information content on cosmological observables, and 2) to provide enough data to train machine learning algorithms. In this paper we describe the simulations and show a few of their applications. We also release the Petabyte of data generated, comprising hundreds of thousands of simulation snapshots at multiple redshifts, halo and void catalogs, together with millions of summary statistics such as power spectra, bispectra, correlation functions, marked power spectra, and estimated probability density functions.

Keywords: large-scale structure of universe – methods: numerical – methods: statistical

1. INTRODUCTION

The discovery of the accelerated expansion of the Universe (Riess et al. 1998; Perlmutter et al. 1999) has revolutionized cosmology. We now believe that $\simeq 70\%$ of the energy content of the Universe is made up of a mysterious substance that is accelerating the expansion of the Universe: dark energy. One of the most important tasks in modern cosmology is to unveil the properties of dark energy. This will help us to understand its nature and improve our knowledge on fundamental physics.

The spatial distribution of matter in the Universe is sensitive to the nature of dark energy, but also to other

fundamental quantities such as the properties of dark matter, the sum of neutrino masses, and the initial conditions of the Universe. Thus, one of the most powerful ways to learn about fundamental physics, is by extracting that information from the large-scale structure of the Universe. This is the goal of many upcoming cosmological missions such as DESI², Euclid³, LSST⁴, PFS⁵, SKA⁶, and WFIRST⁷.

² <https://www.desi.lbl.gov>

³ <https://www.euclid-ec.org>

⁴ <https://www.lsst.org>

⁵ <https://pfs.ipmu.jp/index.html>

⁶ <https://www.skatelescope.org>

⁷ <https://wfirst.gsfc.nasa.gov/index.html>

[†] villaescusa.francisco@gmail.com

The traditional way to retrieve information from cosmological observations is to compare summary statistics from data against theory predictions. An important question is then: What statistic or statistics should be used to extract the maximum information⁸ from cosmic observations?

It is well known that a Gaussian density field can be fully described by its power spectrum or correlation function (see e.g. Verde 2007; Wandelt 2013; Leclercq et al. 2014). This is the main reason why the power spectrum/correlation function is the most prominent statistic employed when analyzing cosmological data: at high-redshift, or on sufficiently large-scales at low-redshift, the Universe resembles a Gaussian density field, and most of the information embedded on it can be extracted from the power spectrum/correlation function.

The cosmic microwave background (CMB) is an example of a Gaussian density field⁹. All the information embedded in it can thus be retrieved through the power spectrum. Notice that for simplicity we are ignoring the non-Gaussian information that can be extracted from the CMB, e.g. through CMB lensing. Currently, some of the tightest and more robust constraints on the value of the cosmological parameters arise from CMB data (Planck Collaboration et al. 2018). Unfortunately, the primary CMB is limited to a plane on the sky at high-redshift, and is insensitive to low-redshift phenomena such as the transition from the matter dominated epoch to the Dark Energy dominated epoch.

Since the number of modes in 3-dimensional surveys is potentially much larger than in CMB observations, it is expected that the constraining power of those surveys will surpass those of CMB observations. Unfortunately, in 3-dimensional surveys, most of the modes are on mildly to non-linear scales. In the regime where the density field is non-Gaussian, it is currently unknown what is the statistic or set of statistics that will allow to extract the maximum information from those modes. From a formal perspective, that question is also mathematically intractable. Being able to extract the cosmological information embedded into non-linear modes will enable us to tighten the value of the cosmological parameters and therefore to improve our understanding of fundamental physics.

One way to tackle this problem is to consider a given statistic/statistics and quantify the information content on it, from linear to non-linear scales. Numerical simulations are needed in this case, as they are one of the most powerful ways to obtain theory predictions in the fully non-linear regime, in real- and redshift-space, for any considered statistic. This is the motivation that brought us to develop the QUIJOTE simulations; we designed them to allow the community to easily quantify the information content on different statistics into the fully non-linear regime.

Another way to approach the problem is to use advanced statistical techniques, such as machine/deep learning, to identify new and optimal statistics to extract cosmological information (Ravanbakhsh et al. 2017;

Charnock et al. 2018; Alsing et al. 2019). One of the requirements of these methods is to have a sufficiently large dataset to train the algorithms. The QUIJOTE simulations have been designed to provide the community with a very big dataset of cosmological simulations.

In this paper we present the QUIJOTE suite; the largest set of full N-body simulations¹⁰ run at this mass and spatial resolution to-date. The QUIJOTE simulations contain 43100 full N-body simulations, expanding more than 7000 cosmological models and at a single redshift, contain more than 8.5 trillion particles. The computational cost of the simulations exceeds 35 million CPU hours, and over 1 Petabyte of data was generated.

This paper is organized as follows. In Section 2 we describe in detail the QUIJOTE simulations. We outline the data products generated by the simulations in Section 3. We present a few applications of the QUIJOTE simulations in Section 4. In Section 5 we show several convergence tests in order to quantify the limitations of the simulations. Finally, we draw our conclusions in Section 6.

2. SIMULATIONS

All the simulations in the QUIJOTE suite are N-body simulations. They have been run using the TreePM code GADGET-III, an improved version of GADGET-II (Springel 2005).

The initial conditions of all simulations are generated at $z = 127$. We obtain the input matter power spectrum and transfer functions by rescaling the $z = 0$ matter power spectrum and transfer functions from CAMB (Lewis et al. 2000). For models with massive neutrinos we use the rescaling method developed in Zennaro et al. (2017), while for models with massless neutrinos we employ the traditional scale-independent rescaling

$$P_m(k, z_i) = \left(\frac{D(z_i)}{D(z)} \right)^2 P_m(k, z = 0), \quad f(z_i) \simeq \Omega_m^\gamma(z_i), \quad (1)$$

where $D(z)$ is the growth factor at redshift z , f is the growth rate and $\gamma \simeq 0.6$ for Λ CDM. From the input matter power spectrum and transfer functions we compute displacements and peculiar velocities employing the Zeldovich approximation (Zel'dovich 1970) (for cosmologies with massive neutrinos) or second order perturbation theory (for cosmologies with massless neutrinos). The displacements and peculiar velocities are then assigned to particles that are initially laid on a regular grid. In models with massive neutrinos we use two different grids that are offset by half a grid size: one grid for CDM and one grid for neutrinos. For 2LPT, we use the code in <https://cosmo.nyu.edu/roman/2LPT/>, while for neutrinos we used a modified version of N-GenIC, publicly available at https://github.com/franciscovillaescusa/N-GenIC_growth. The rescaling code used for massive neutrino cosmologies is publicly available in <https://github.com/matteozennaro/reps>.

All simulations have a cosmological volume of $1 (h^{-1}\text{Gpc})^3$. The majority of the simulations follow the evolution of 512^3 CDM particles (plus 512^3 for simulations with massive neutrinos): our *fiducial-resolution*. We however also have simulations with 256^3

⁸ By information we mean the constraints on the value of the cosmological parameters.

⁹ To-date, there is no significant evidence that points towards the CMB being non-Gaussian (Planck Collaboration et al. 2019).

¹⁰ To the best of our knowledge.

(*low-resolution*) and 1024^3 (*high-resolution*) CDM particles. The gravitational softening length is set to $1/40$ of the mean interparticle distance, i.e. 100, 50 and 25 $h^{-1}\text{kpc}$ for the low-, fiducial- and high-resolution simulations, respectively. The gravitational softening is the same for CDM and neutrino particles. We save snapshots at redshifts 0, 0.5, 1, 2, and 3. We also save the initial conditions and the scripts to generate them.

Table 1 summarizes the main features of all the QUIJOTE simulations.

2.1. Simulations with massive neutrinos

In simulations with massive neutrinos, we use the traditional particle-based method (Brandbyge et al. 2008; Viel et al. 2010) to model the cosmic neutrino background. In that method, neutrinos are described as a collisionless and pressureless fluid, that is discretized into a set of neutrino particles. Those particles are assigned thermal velocities (on top of peculiar velocities) that are randomly drawn from their Fermi-Dirac distribution at the simulation starting redshift.

One of the well-known problems of this method, is that a significant fraction of the neutrino particles will cross the simulation box several times (due to their large thermal velocities). This will erase the clustering of neutrinos on small scales, producing a white power spectrum (or shot-noise). This effect is however negligible on most of the observational quantities, e.g. the total matter power spectrum, the halo/galaxy power spectrum.

New methods have been developed to address this problem (see e.g. Banerjee et al. 2018). The 5000 simulations of the LHVW latin-hypercube have been run using this method, that provides a neutrino density field with a negligible level of shot-noise.

2.2. Paired fixed simulations

The QUIJOTE simulations contain a) standard, b) fixed and c) paired fixed simulations. The differences between those is the way the initial conditions are generated. Consider a Fourier-space mode, $\delta(\vec{k})$. Since it is in general a complex number, we can write it as $\delta(\vec{k}) = Ae^{i\theta}$, where both the amplitude A , and the phase θ , depends on the considered wavenumber \vec{k} . For Gaussian density fields, A follows a Rayleigh distribution and θ is drawn from an uniform distribution between 0 and 2π . This is the standard way to generate initial conditions for cosmological simulations. In fixed simulations, while θ is still drawn from a uniform distribution between 0 and 2π , the value of A is fixed to the square root of the variance of the previous Rayleigh distribution. Finally, paired fixed simulations are two fixed simulations where the phases of the two pairs differ by π . We refer the reader to Pontzen et al. (2016); Angulo & Pontzen (2016); Villaescusa-Navarro et al. (2018) for further details.

Fixed and paired fixed simulations have received a lot of attention recently, since it has been shown that they can significantly reduce the amplitude of cosmic variance on different statistics (e.g. the power spectrum) without inducing a bias on the results (Pontzen et al. 2016; Angulo & Pontzen 2016; Villaescusa-Navarro et al. 2018; Anderson et al. 2018; Chuang et al. 2019; Klypin et al. 2019). While these simulations can not be used to estimate covariance matrices, they may be useful to compute

numerical derivatives, or to provide an effective larger cosmological volume. For this reason, some of the simulations we have run are fixed and paired fixed.

2.3. Fiducial cosmology

The value of the cosmological parameters for our fiducial model are: $\Omega_m = 0.3175$, $\Omega_b = 0.049$, $h = 0.6711$, $n_s = 0.9624$, $\sigma_8 = 0.834$, $M_\nu = 0.0\text{ eV}$, and $w = -1$. The values of those parameters are in good agreement with the latest constraints by Planck (Planck Collaboration et al. 2018).

For this model, we have run a total 17100 simulations. Of those, 15000 are standard simulations run at the fiducial resolution with 2LPT initial conditions. The main purpose of these simulations is to compute covariance matrices. We also have a set of 500 paired fixed simulations, with 2LPT initial conditions at fiducial resolution that can be used to study properties of paired fixed simulations and to compute numerical derivatives.

Furthermore, we have a set of 500 standard simulations with Zel'dovich initial conditions at fiducial resolution needed to compute the derivatives with respect to neutrino masses (see subsection 5.1). Finally, a set of 1000 standard simulations at low-resolution, and 100 standard simulations at high-resolution are available to carry out resolution tests and apply super-resolution techniques (see subsection 4.6).

2.4. Simulations for numerical derivatives

One of the ingredients needed to quantify the information content of a statistic is the partial derivatives of it with respect to the cosmological parameters (see subsection 4.1). For Ω_m , Ω_b , h , n_s , σ_8 , and w we compute partial derivatives as

$$\frac{\partial \vec{S}}{\partial \theta} \simeq \frac{\vec{S}(\theta + d\theta) - \vec{S}(\theta - d\theta)}{2d\theta}, \quad (2)$$

where \vec{S} is the considered statistic (e.g. the matter power spectrum at different wavenumbers), and θ is the cosmological parameter. We thus need to evaluate the statistic on simulations where only the considered parameter is varied above and below its fiducial value. In order to fulfill this requirement, we have run simulations varying only one cosmological parameter at a time. For instance, the simulations coined Ω_m^+/Ω_m^- have the same value Ω_b , h , n_s , σ_8 , M_ν and w as the fiducial model but the value of Ω_m is slightly larger/smaller. In this case $d\Omega_m/\Omega_m \simeq 1.8\%$: $\Omega_m = 0.3275$ for Ω_m^+ and $\Omega_m = 0.3075$ for Ω_m^- .

In the simulations Ω_b^{++} and Ω_b^{--} we vary Ω_b by $d\Omega_b/\Omega_b \simeq 4\%$. While when varying the others parameters h , n_s , σ_8 and w we have $dh/h \simeq 3\%$, $dn_s/n_s \simeq 2\%$, $d\sigma_8/\sigma_8 \simeq 1.8\%$, $dw/w = 5\%$, respectively. These numbers were chosen such as the difference is small enough to approximate the derivatives, but not too small to be dominated by numerical noise. In the Ω_b^+ and Ω_b^- simulations we have $d\Omega_b/\Omega_b \simeq 2\%$. For most of the statistics we have considered, this difference is too small and the derivatives are slightly affected by numerical noise.

For all these models, we have run 500 standard simulations and 500 paired fixed simulations using 2LPT at the fiducial resolution. The exception is the models with

Name	Ω_m	Ω_b	h	n_s	σ_8	M_ν (eV)	w	realizations	simulations	ICs	$N_c^{1/3}$	$N_\nu^{1/3}$
Fid	<u>0.3175</u>	<u>0.049</u>	<u>0.6711</u>	<u>0.9624</u>	<u>0.834</u>	<u>0</u>	<u>-1</u>	15000	standard	2LPT	512	0
								500	standard	Zeldovich	512	0
								500	paired fixed	2LPT	512	0
								1000	standard	2LPT	256	0
								100	standard	2LPT	1024	0
Ω_m^+	<u>0.3275</u>	0.049	0.6711	0.9624	0.834	0	-1	500	standard	2LPT	512	0
Ω_m^-	<u>0.3075</u>	0.049	0.6711	0.9624	0.834	0	-1	500	paired fixed	2LPT	512	0
Ω_b^{++}	0.3175	<u>0.051</u>	0.6711	0.9624	0.834	0	-1	500	standard	2LPT	512	0
Ω_b^+	0.3175	<u>0.050</u>	0.6711	0.9624	0.834	0	-1	500	paired fixed	2LPT	512	0
Ω_b^-	0.3175	<u>0.048</u>	0.6711	0.9624	0.834	0	-1	500	paired fixed	2LPT	512	0
Ω_b^{--}	0.3175	<u>0.047</u>	0.6711	0.9624	0.834	0	-1	500	standard	2LPT	512	0
h^+	0.3175	0.049	<u>0.6911</u>	0.9624	0.834	0	-1	500	standard	2LPT	512	0
h^-	0.3175	0.049	<u>0.6511</u>	0.9624	0.834	0	-1	500	paired fixed	2LPT	512	0
n_s^+	0.3175	0.049	0.6711	<u>0.9824</u>	0.834	0	-1	500	standard	2LPT	512	0
n_s^+	0.3175	0.049	0.6711	<u>0.9424</u>	0.834	0	-1	500	paired fixed	2LPT	512	0
σ_8^+	0.3175	0.049	0.6711	0.9624	<u>0.849</u>	0	-1	500	standard	2LPT	512	0
σ_8^-	0.3175	0.049	0.6711	0.9624	<u>0.819</u>	0	-1	500	paired fixed	2LPT	512	0
M_ν^{+++}	0.3175	0.049	0.6711	0.9624	0.834	<u>0.4</u>	-1	500	standard	Zeldovich	512	512
M_ν^{++}	0.3175	0.049	0.6711	0.9624	0.834	<u>0.2</u>	-1	500	paired fixed	Zeldovich	512	512
M_ν^+	0.3175	0.049	0.6711	0.9624	0.834	<u>0.1</u>	-1	500	standard	Zeldovich	512	512
w^+	0.3175	0.049	0.6711	0.9624	0.834	0	<u>-1.05</u>	500	paired fixed	Zeldovich	512	0
w^-	0.3175	0.049	0.6711	0.9624	0.834	0	<u>-0.95</u>	500	standard	Zeldovich	512	0
LH	[0.1 , 0.5]	[0.03 , 0.07]	[0.5 , 0.9]	[0.8 , 1.2]	[0.6 , 1.0]	0	-1	2000	standard	2LPT	512	0
								2000	fixed		512	
								2000	standard		1024	
LH νw	[0.1 , 0.5]	[0.03 , 0.07]	[0.5 , 0.9]	[0.8 , 1.2]	[0.6 , 1.0]	[0 , 1]	[-1.3 , -0.7]	5000	standard	Zeldovich	512	512
total	-	-	-	-	-	-	-	43100	-	-	-	-
	-	-	-	-	-	-	-	-	-	-	19696	10240

Table 1

Characteristics of the QUIJOTE simulations. The simulations in the first block have been designed to quantify the information content on cosmological observables. They have a large number of realizations for a fiducial cosmology (needed to estimate the covariance matrix) and simulations varying just one cosmological parameter at a time (needed to compute numerical derivatives). The simulations in the second block arise from latin-hypercubes expanding a large volume in parameter space. The initial conditions of all simulations were generated at $z = 127$ using 2LPT, except for the simulations with massive neutrinos, where we used the Zel'dovich approximation. All simulations have a volume of $1 (h^{-1}\text{Gpc})^3$ and we have three different resolutions: low-resolution (256^3 particles), fiducial-resolution (512^3 particles) and high-resolution (1024^3 particles). In the simulations with massive neutrinos we assume three degenerate neutrino masses. Simulations have been run with the TreePM+SPH GADGET-III code. We save snapshots at redshifts 3, 2, 1, 0.5 and 0.

$w \neq -1$ where we only run 500 standard simulations and Ω_b^+/Ω_b^- that only have 500 paired fixed simulations.

To compute numerical derivatives with respect to massive neutrinos, we cannot use Eq. 2, since the second term in the numerator will correspond to a Universe with negative neutrino masses¹¹. For this reason, we have run simulations at several values of the neutrino masses: $M_\nu^+ = 0.1$ eV, $M_\nu^{++} = 0.2$ eV and $M_\nu^{+++} = 0.4$ eV. From these simulations, several derivatives can be com-

puted

$$\begin{aligned} \frac{\partial \vec{S}}{\partial M_\nu} &\simeq \frac{\vec{S}(M_\nu) - \vec{S}(M_\nu = 0)}{M_\nu} \\ \frac{\partial \vec{S}}{\partial M_\nu} &\simeq \frac{-\vec{S}(2M_\nu) + 4\vec{S}(M_\nu) - 3\vec{S}(M_\nu = 0)}{2M_\nu} \\ \frac{\partial \vec{S}}{\partial M_\nu} &\simeq \frac{\vec{S}(4M_\nu) - 12\vec{S}(2M_\nu) + 32\vec{S}(M_\nu) - 21\vec{S}(M_\nu = 0)}{12M_\nu} \end{aligned}$$

where the first equation can be used for $M_\nu = 0.1, 0.2$ or 0.4 eV. The second equation can instead be evaluated with $M_\nu = 0.1$ or 0.2 eV while the last equation requires $M_\nu = 0.1$ eV. Notice that if the differences between the fiducial model and the cosmology with 0.1 eV neutrinos are not dominated by noise, the last equation

¹¹ Notice that our fiducial cosmology is for a Universe with massless neutrinos.

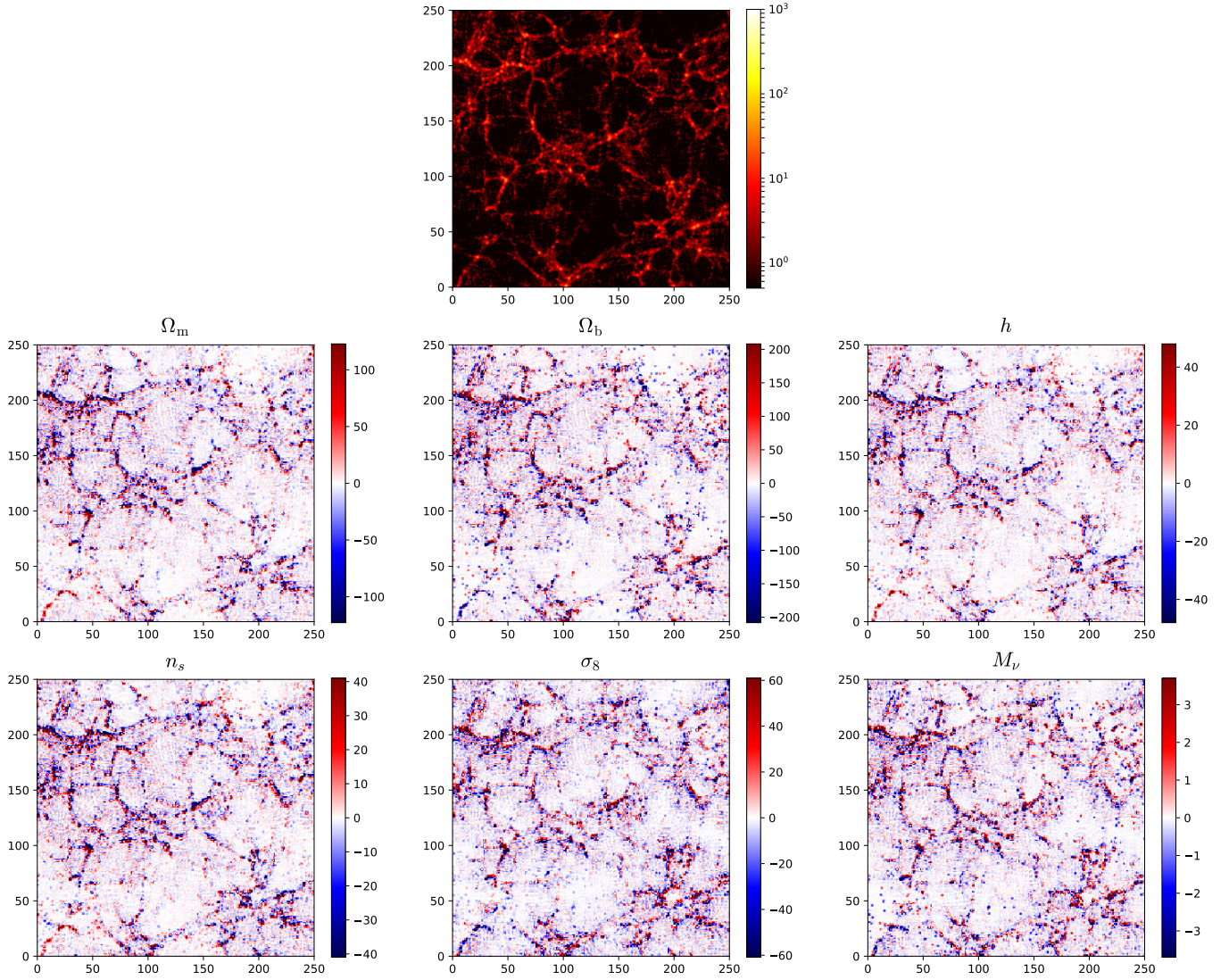


Figure 1. The image on the top shows the large-scale structure in a region of $250 \times 250 \times 15 (h^{-1}\text{Mpc})^3$ at $z = 0$ for the fiducial cosmology. We have taken simulations with the same random seed but different values of just one single parameter, and used them to compute the derivative of the density field with respect to the parameters. The panels on the middle and bottom row show those derivatives with respect to Ω_m (middle-left), Ω_b (middle-center), h (middle-right), n_s (bottom-left), σ_8 (bottom-middle), and M_ν (bottom-right). It can be seen how different parameters affect the large-scale structure in different manners.

will provide the most precise estimation of the derivative. In some cases, e.g. with the halo mass function, differences between the fiducial model with massless neutrinos and cosmology with 0.1 eV neutrinos is too small, and therefore dominated by noise. In these cases, it is recommended to use the above second equation with $M_\nu = 0.2$ eV.

For the models with 0.1 eV, 0.2 eV and 0.4 eV we have run 500 standard and 500 paired fixed simulations at the fiducial resolution. As stated above, for models with massive neutrinos, the initial conditions have been generated using the Zel'dovich approximation.

The top panel of Fig. 1 shows the spatial distribution of matter in a realization of the fiducial cosmology. The other panels show the derivative of the density field of that particular realization with respect to the parameters Ω_m , Ω_b , h , n_s , σ_8 , and M_ν .

2.5. Latin-hypercubes

Besides the simulations described above, we have also run a set of 11000 simulations on different latin-hypercubes. The main purpose of these simulations is to provide enough data to train machine learning algorithms. In Section 4 we outline some applications of these simulations.

The simulations can be split into two main sets. In the first one, called LH, we use a latin-hypercube where we vary the value of Ω_m between 0.1 and 0.5, Ω_b between 0.03 and 0.07, h between 0.5 and 0.9, n_s between 0.8 and 1.2, σ_8 between 0.6 and 1.0 and keep fixed M_ν to 0.0 eV and w to -1. LH is made of three different sets, but the value of the cosmological parameters is the same among the three set. The first one, is made of standard simulations with different random seeds. The second one, is made of fixed simulations, all of them having the same random seed. Those two sets have been

run at the fiducial resolution. The last set is made of standard simulations with different random seeds but at high-resolution: 1024^3 CDM particles. The initial conditions of all these simulations were generated with 2LPT. The three different sets contain 2000 simulations each. The set with fixed simulations can be used to create an accurate emulator, while the other two sets can be used to train machine learning algorithms accounting for the presence of cosmic variance.

The second latin-hypercube, called LH ν w, is a set 5000 standard simulations with different random seeds where the value of the cosmological parameters is changed within: $\Omega_m \in [0.1, 0.5]$, $\Omega_b \in [0.03, 0.07]$, $h \in [0.5, 0.9]$, $n_s \in [0.8, 1.2]$, $\sigma_8 \in [0.6, 1.0]$, $M_\nu \in [0, 1]$, $w \in [-1.3, -0.7]$. Since these simulations contain massive neutrinos, the initial conditions were generated using the Zel'dovich approximation. All the simulations follow the evolution of 512^3 CDM particles plus 512^3 neutrino particles. Each simulation is run with a different random seed.

Fig. 2 shows the spatial distribution of matter in 6 different cosmological models of the high-resolution LH simulations at $z = 0$. Different features show up in the different images: from very long and thick filaments to highly clustered structures. This reflects the broad range covered by the QUIJOTE simulations in the parameter space; from realistic models to extreme scenarios.

3. DATA PRODUCTS

In this section we describe the data products of the QUIJOTE simulations.

3.1. Snapshots

We provide access to the full snapshots of the simulations at redshifts 0, 0.5, 1, 2, 3, and the initial conditions at $z = 127$. The snapshots only have four different fields, 1) header, 2) positions, 3) velocities and 4) IDs.

The header contains information about the snapshot such as, redshift, value of Ω_m , Ω_Λ , number of particles, number of files...etc. The position block stores the positions of the particles in comoving h^{-1} kpc. The velocities of the particles are in the velocities block while the IDs block hosts the unique ids of the particles. The positions and velocities are saved as 32-bits floats, while the IDs are 32-bits integers. The snapshots are stored in either GADGET-II or hdf5 format. PYLIANS¹² can be used to read the snapshots, independently of the format.

3.2. Halo catalogues

We save halo catalogues at each redshift for all the simulations; a total of 215500 halo catalogues. Halos are identified using the Friends-of-Friends (FoF) algorithm (Davis et al. 1985). We set the value of the linking length parameter to $b = 0.2$. Each halo catalogue contains the positions, velocities, masses and total number of particles of each halo. Only CDM particles are linked in the FoF halos, as the contribution of neutrinos to the total halo mass is expected to be negligible (Villaescusa-Navarro et al. 2011, 2013; Ichiki & Takada 2012; LoVerde & Zaldarriaga 2014). For simulations with large neutrino masses (e.g. the simulations in the LH ν w) we also provide halo catalogues with the mass of halos being CDM

plus neutrinos. The halo catalogues are saved in a binary format. PYLIANS can be used to read the catalogues.

For a subset of the simulations we have also identified halos using the AMIGA halo finder (Knollmann & Knebe 2009).

3.3. Void catalogues

We provide void catalogs from every simulation at each redshift. For simulations with massive neutrinos, we provide two void catalogs - one in which the voids were identified using the total matter field, and the other in which the voids were identified in only the CDM+baryon field. For cosmologies with massless neutrinos, we only provide the latter. More than 250000 void catalogues are thus provided by the QUIJOTE simulations.

Voids are identified in the simulations using the void finder used in Banerjee & Dalal (2016). The algorithm is as follows. First, the relevant overdensity field (CDM or CDM+neutrinos) is computed on a regular grid. This overdensity field is then smoothed on some scale R_{smooth} using a top-hat filter. All voxels at which the value of the smoothed overdensity field is below some threshold $\delta_{\text{threshold}}$ are stored. Note that the initial R_{smooth} is chosen to be quite large ($\sim 100 h^{-1}$ Mpc). The grid voxels are then sorted in order of increasing overdensity, and the voxel with the lowest overdensity (or most underdense) is labelled as a void center with void radius R_{smooth} . Since we use spherical top-hat smoothing, we can also associate a mass with the void: $M_v = 4/3\pi R_{\text{smooth}}^3 \bar{\rho}(1 + \delta_{\text{threshold}})$. We also tag all voxels within radius R_{smooth} so that they cannot later be labelled as void centers. We then work down the list of points which crossed the threshold, i.e. to higher overdensities (less underdense), identifying them as new void centers with radius R_{smooth} if they do not overlap with previously identified voids.

Once all voxels below threshold for a given R_{smooth} have been checked, we move to a smaller value of R_{smooth} and repeat the procedure outlined above. In this way, the largest voids are the first identified, and then progressively smaller voids are found and stored in the void catalog. Note that by this definition, we do not have nested void regions in the provided void catalogs.

By default, our void find was run using $\delta_{\text{threshold}} = -0.7$, but we also provide void catalogues with different values of $\delta_{\text{threshold}}$ such as -0.5 or -0.3. Our void catalogs contain the positions, radii, and void size functions (number density of voids per unit of radius). The void catalogues are stored in HDF5 files.

3.4. Power spectra

We compute power spectra for 1) total matter field, 2) CDM+baryons (only for simulations with massive neutrinos), and 3) halos with different masses. The power spectra are computed for all simulations, at the redshifts 0, 0.5, 1, 2, and 3, and also at $z = 127$ for 1) and 2). We compute the power spectra in both real- and redshift-space. In redshift-space, we place the redshift-space distortions along one cartesian axis, and compute the monopole, quadrupole and hexadecapole. We repeat the procedure for the three cartesian axes, i.e. in redshift-space, we compute three power spectra instead of one. In total, the QUIJOTE simulations contain over 1 million power spectra.

¹² <https://github.com/franciscovillaescusa/Pylians>

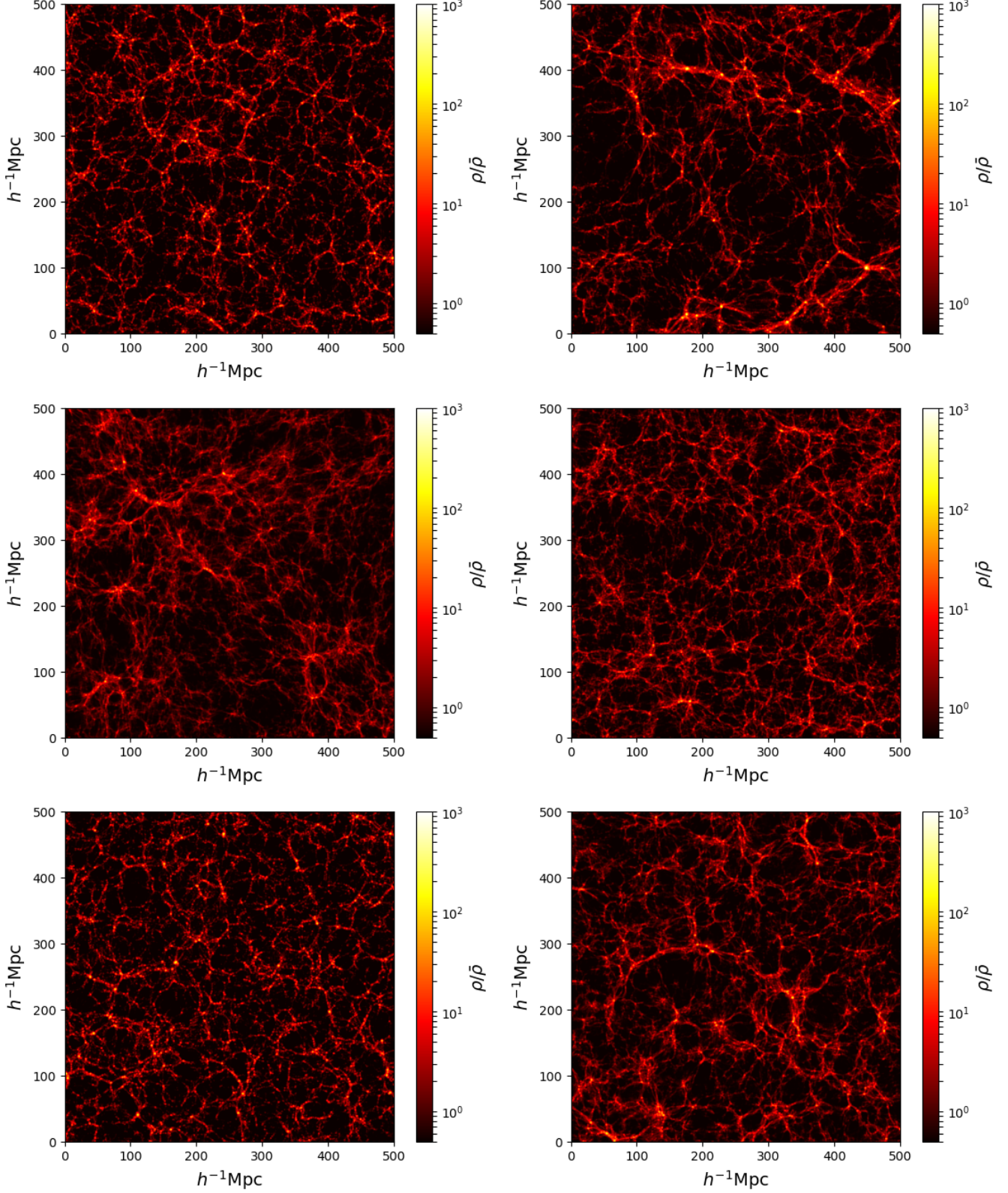


Figure 2. Projected density field of a region of $500 \times 500 \times 10$ ($h^{-1}\text{Mpc}$)³ from 6 different cosmologies of the high-resolution LH simulations at $z = 0$. The top-left panel corresponds to a model close to Planck: $\{\Omega_m, \Omega_b, h, n_s, \sigma_8\} = \{0.3223, 0.04625, 0.7015, 0.9607, 0.8311\}$. The other panels represent cosmologies with $\{0.1005, 0.04189, 0.5133, 1.0107, 0.9421\}$ (top-right), $\{0.1029, 0.06613, 0.7767, 1.0115, 0.6411\}$ (middle-left), $\{0.1645, 0.05257, 0.7743, 1.0311, 0.6149\}$ (middle-right), $\{0.4487, 0.03545, 0.5167, 1.0387, 0.9291\}$ (bottom-left), $\{0.1867, 0.04503, 0.6189, 0.8307, 0.7187\}$ (bottom-right).

3.5. Marked power spectra

Marked correlation functions are special 2-point statistics were correlations are weighted according to a mark, e.g. some environmental property. They have been shown to be interesting tools to study galaxy clustering dependence on galaxy properties such as morphology, luminosity, etc. (Beisbart & Kerscher 2000; Sheth et al. 2005), halo clustering dependence on merger history (Gottloeber et al. 2002), modified theories of gravity (White 2016; Valogiannis & Bean 2018; Armijo et al. 2018; Hernández-Aguayo et al. 2018), and neutrinos' masses (Massara et al. 2019).

We compute marked power spectra of the matter density field, which are the Fourier counterpart of marked correlations. Inspired by White (2016), we consider the mark $M(\vec{x})$ of the form

$$M(\vec{x}) = \left[\frac{1 + \delta_s}{1 + \delta_s + \delta_R(\vec{x})} \right]^p, \quad (3)$$

that depends on the local matter density $\delta_R(\vec{x})$, a parameter δ_s , and an exponent p . The density $\delta_R(\vec{x})$ is obtained by smoothing the matter density field with a Top-Hat filter at scale R and can be evaluated at each point in the space \vec{x} . Thus, the mark depends on three parameters: R , p , and δ_s . When $\delta_s \rightarrow 0$, $M(\vec{x}) \rightarrow [\bar{\rho}/\rho_R(\vec{x})]^p$ with $\bar{\rho}$ being the mean matter density of the Universe and $\rho_R(\vec{x})$ the density inside a sphere of radius R around \vec{x} . If $p > 0$ the mark gives more weight (and therefore more importance) to points that are in underdense regions, while if $p < 0$ points in overdensities are weighted more. One can adjust these parameters to obtain different types of marks, that can weight in different ways the various components of the large-scale structure.

The marked power spectra are computed as follows. Firstly, the smoothed density field $\delta_R(\vec{x})$ is calculated on the vertex of a grid; the values of δ_R at the position of each matter particle are then computed via interpolation and a mark is assigned to each particle. Secondly, the marked power spectrum is computed as a power spectrum with each particle weighted by its mark.

We consider 5 different values for each of the three mark parameters: $R = 5, 10, 15, 20, 30 h^{-1} \text{Mpc}$, $p = -1, 0.5, 1, 2, 3$ and $\delta_s = 0, 0.25, 0.5, 0.75, 1$, giving a total of 125 different mark models. In total, millions of marked power spectra are available in the QUIJOTE simulations.

3.6. Correlation functions

We compute correlation functions for 1) total matter field and 2) CDM+baryons field (only for simulations with massive neutrinos). The correlation functions are computed at redshifts 0, 0.5, 1, 2, and 3, in both real- and redshift-space. In the same way as for the power spectrum, redshift-space distortions are placed along one cartesian axis and three correlation functions are computed, one for each axis.

The procedure we use to compute the correlation functions is as follows. First, we assign particle masses to a regular grid with N^3 cells using the Cloud-in-Cell (CIC) mass assignment scheme and compute the density contrast: $\delta(\vec{x}) = \rho(\vec{x})/\bar{\rho} - 1$. We then Fourier transform the density contrast field to get $\delta(\vec{k})$. Next, we compute

the modulus of each Fourier mode, $|\delta(\vec{k})|^2$, and Fourier transform back that field. Finally, we compute the correlation function by averaging modes that fall within a given radius interval. In redshift-space, the quadrupole and hexadecapole are computed in the same way as the monopole by weighing each mode by the contribution of the corresponding Bessel function.

By default we set N to be equal to the cubic root of the number of particles in the simulation, but we also compute correlation functions in finer grids. In total, we provide over 1 million correlation functions.

3.7. Bispectra

We compute bispectra for the total matter field as well as for halo catalogs in both real- and redshift-space at redshifts 0, 0.5, 1, 2 and 3. We use a Fast Fourier Transform (FFT) based estimator similar to the estimators described in Sefusatti & Scoccimarro (2005), Scoccimarro (2015), and Sefusatti et al. (2016). We first interpolate matter particles/halos to a grid to compute the density contrast field, $\delta(\vec{x})$, using a fourth-order interpolation to get interlaced grids and then Fourier transform the grid to get $\delta(\vec{k})$. We then measure the bispectrum monopole using

$$B_0(k_1, k_2, k_3) = \frac{1}{V_B} \int_{k_1} d^3 q_1 \int_{k_2} d^3 q_2 \int_{k_3} d^3 q_3 \delta_D(\mathbf{q}_{123}) \times \delta(\mathbf{q}_1) \delta(\mathbf{q}_2) \delta(\mathbf{q}_3) - B^{\text{SN}} \quad (4)$$

where δ_D is the Dirac delta function, V_B is a normalization factor proportional to the number of triplets in the triangle bin defined by k_1 , k_2 , and k_3 , and B^{SN} is the correction for Poisson shot noise. To evaluate the integral, we take advantage of the plane-wave representation of δ_D . For more details, we refer readers to Hahn et al. (2019)¹³. We use $\delta(\vec{x})$ grids with $N_{\text{grid}} = 360$ and triangle configurations defined by k_1 , k_2 , and k_3 bins of width $\Delta k = 3k_f = 0.01885 h \text{Mpc}^{-1}$. For $k_{\text{max}} = 0.5 h \text{Mpc}^{-1}$ there are 1898 triangle configurations. Redshift-space distortions are imposed along one Cartesian axis, same as the power spectrum, so we measure three bispectra, one for each axis.

In total, the QUIJOTE simulations provide over 1 million bispectra.

3.8. PDFs

We estimate the probability density functions (PDF) of the matter, CDM+baryons and halo field in all the simulations at all redshifts. The PDFs are computed as follows. First, we deposit particle masses (or halo positions) to a regular grid with N^3 cells using the Cloud-in-Cell (CIC) mass assignment scheme. We then smooth that field with a Gaussian filter of radius, R . Finally, the PDF is calculated by computing the fraction of cells whose overdensity lie within a given interval. We compute the PDFs for many different values of R . By default we take N to be the cubic root of the number of CDM particles in the simulation. In total, the QUIJOTE simulations provide more than 1 million PDFs.

¹³ The code that we use to evaluate B_0 is publicly available at <https://github.com/changhoonhahn/pySpectrum>

4. APPLICATIONS

The QUIJOTE simulations have been designed to address two main goals: 1) to quantify the information content on cosmological observables, and 2) to provide enough statistics to train machine learning algorithms. In this section we describe a few examples of applications of the simulations.

4.1. Information content from observables

As discussed in the introduction, it is currently unknown what statistic or statistics should be used to retrieve the maximum cosmological information from non-Gaussian density fields. One way to quantify the information content on a set of cosmological parameters, $\vec{\theta}$, given a statistics \vec{S} , is through the Fisher matrix formalism. The Fisher matrix is defined as

$$F_{ij} = \sum_{\alpha, \beta} \frac{\partial S_{\alpha}}{\partial \theta_i} C_{\alpha\beta}^{-1} \frac{\partial S_{\beta}}{\partial \theta_j}, \quad (5)$$

where S_i is the element i of the statistic \vec{S} and C is the covariance matrix

$$C_{\alpha\beta} = \langle (S_{\alpha} - \bar{S}_{\alpha})(S_{\beta} - \bar{S}_{\beta}) \rangle; \quad \bar{S}_i = \langle S_i \rangle. \quad (6)$$

Notice that in Eq. 5 we have set to 0 the term (see e.g. Tegmark et al. 1997)

$$\frac{1}{2} \text{Tr} \left[C^{-1} \frac{\partial C}{\partial \theta_{\alpha}} C^{-1} \frac{\partial C}{\partial \theta_{\beta}} \right]. \quad (7)$$

This is because this term is expected to be small (Kodwani et al. 2019) but including it will also lead to an underestimation of the parameter errors (Carron 2013; Alsing & Wandelt 2018).

The error on the parameter θ_i , marginalized over the other parameters, is given by

$$\delta\theta_i \geq \frac{1}{\sqrt{(F^{-1})_{ii}}}. \quad (8)$$

Thus, in order to quantify the constraints that a given statistic can place on the value of the cosmological parameters we only need two ingredients: 1) the covariance matrix of the statistic(s) and 2) the derivatives of the statistic(s) with respect to the cosmological observables. As discussed in detail in Sec. 2, the QUIJOTE simulations have been designed to numerically evaluate those two pieces.

In this paper we consider one of the simplest applications of our simulations: the information content on the matter power spectrum. In Fig. 3 we plot the correlation matrix of the matter power spectrum at $z = 0$, defined as

$$\frac{C_{k_i k_j}}{\sqrt{C_{k_i k_i} C_{k_j k_j}}} \quad (9)$$

when computed using 100 (left), 1000 (middle) and 15000 (right) realizations of the fiducial cosmology. As can be seen, results are noisy when computing the covariance with few realizations; this in turn, affects the results of the Fisher matrix analysis.

As it is well-known, on large-scales, the different Fourier modes are decoupled, and the covariance matrix

is almost diagonal. On small-scales, modes with different wavenumbers are coupled, giving rise to non-diagonal elements, whose amplitude increases on smaller scales. Notice that previous works have investigated in detail the properties of the covariance matrix using a very large set of simulations (Blot et al. 2015, 2016).

In Fig. 4 we show the second ingredient we need to evaluate the Fisher matrix: the partial derivatives of the matter power spectrum with respect to the cosmological parameters. In our case, we only consider Ω_m , Ω_b , h , n_s , σ_8 , and M_{ν} , and show results at $z = 0$. In that Figure we show the derivatives when computed using different number of realizations. It can be seen how results are well converged, all the way to $k = 1 \text{ hMpc}^{-1}$. We can also see how the derivatives are different among parameters, pointing out that the matter power spectrum alone can provide information on each parameter separately.

With the covariance matrix and the derivatives we can evaluate the Fisher matrix and determine the constraints on the cosmological parameters. We have verified that our results are converged, i.e. constraints do not change if the covariance and derivatives are evaluated with less realizations. We have also checked that our results are robust against different evaluations of the neutrino derivatives. We show the results on Fig. 5 when we consider the matter power spectrum down to $k_{\text{max}} = 0.1$ (red), 0.2 (blue) and 0.5 (green) hMpc^{-1} . As expected, the smaller the scales, the more cosmological information we can extract and the tighter the constraints on the parameters. However, the gain with scale does not scale proportional to k_{max}^3 , as naively expected just by counting number of modes. There are two main reasons for this behaviour: 1) the covariance becomes non-diagonal on small scales; modes become correlated and therefore the number of independent modes do not scale as k_{max}^3 , and 2) degeneracies among parameters limit the amount of information that can be extracted.

In Fig. 6 we show the marginalized 1σ constraints on the value of the cosmological parameters as a function of k_{max} . As can be seen, the constraints on the parameters tend to saturate on small scales. We note that this result is mainly driven by degeneracies among parameters rather than the covariance becoming non-diagonal.

The cosmological information that was present on the matter power spectrum at high-redshift on small scales has now leaked into other statistics due to non-linear gravitational evolution. The QUIJOTE simulations can be used to quantify it. The information content on the full halo bispectrum in redshift-space is estimated in Hahn et al. (2019). The constraints on the parameters by combining the power spectrum, halo mass function and void size function is presented in Villaescusa-Navarro et al. (2019), while sensitivity of the cosmological parameters to the marked power spectrum is shown in Massara et al. (2019).

4.2. Information content from neural nets

A way of searching for new statistics is using information maximising neural networks (IMNN) (Charnock et al. 2018). The IMNN is designed to automatically find informative, non-linear summaries of the data. The method uses neural networks to transform non-Gaussian data in to the set of optimally compressed, Gaussianly-

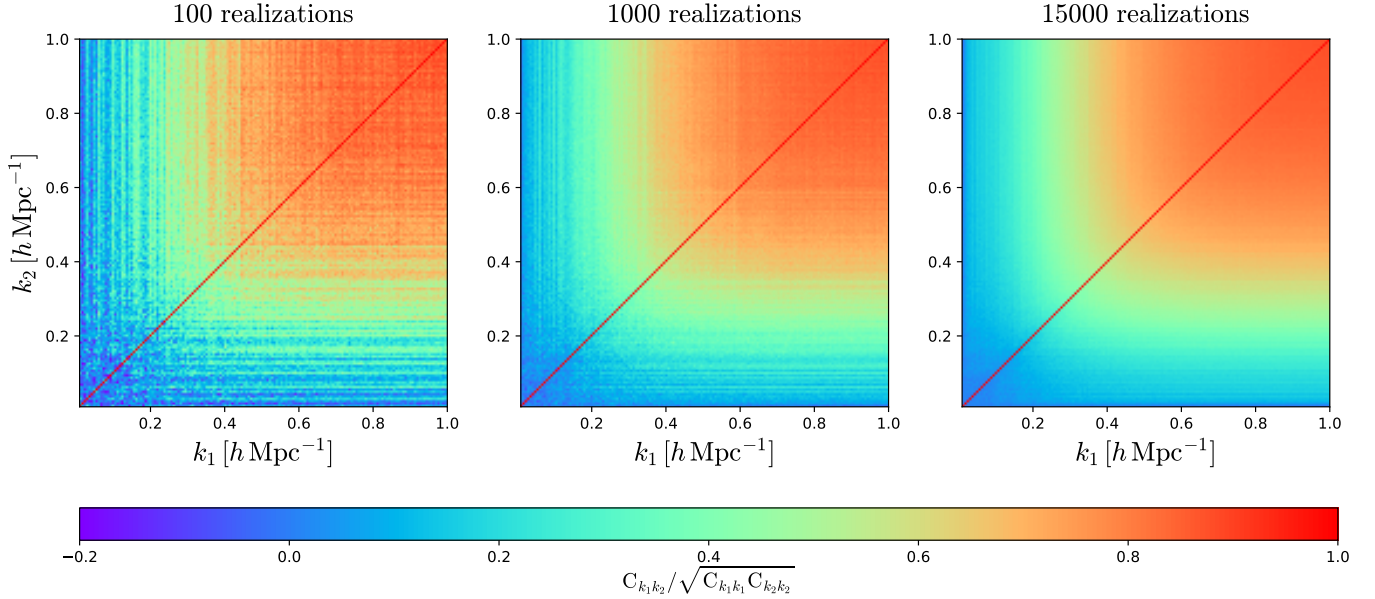


Figure 3. Correlation matrix of the matter power spectrum at $z = 0$ computed using 100 (left), 1000 (center), and 15000 (right) realizations. On large-scales, modes are decoupled, so correlations are small. On small scales, modes are tightly coupled, and the amplitude of the correlation is high. As expected, the noise in the covariance matrix shrinks with the number of realizations.

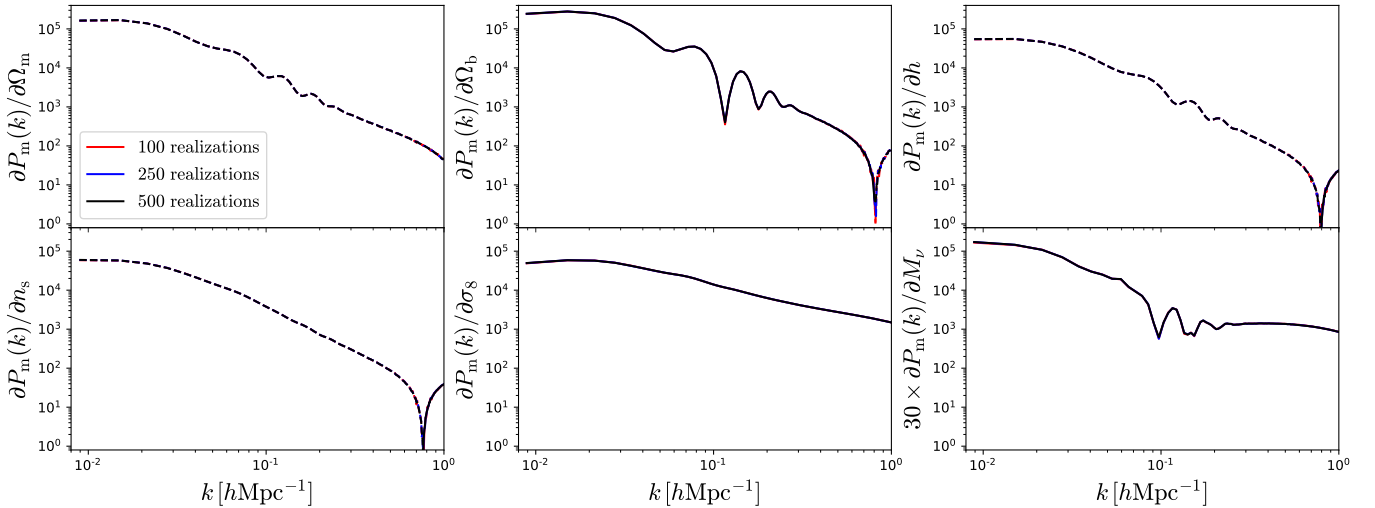


Figure 4. Derivatives of the matter power spectrum in real-space with respect to Ω_m (upper-left), Ω_b (upper-middle), h (upper-right), n_s (bottom-left), σ_8 (bottom-middle), and M_ν (bottom-right) at $z = 0$. Solid and dashed lines represent positive and negative values of the derivatives, respectively. We show the derivatives when computed using 100 (red), 250 (blue), and 500 (black) realizations. It can be seen how results are very converged against the number of realizations.

distributed summaries via maximisation of the Fisher information. These summaries can then be used in a likelihood-free inference setting or even directly as pseudo-maximum likelihood estimators of the parameters. By building neural networks using physically motivated principles, not only will we obtain informative summaries of the data, but we will be able to attribute these summaries to real space effects, hence learning even more about the connection between data and the underlying cosmological model. As an input, the IMNN requires simulated data to compute the covariance of the summaries and the derivative of the summaries with respect to model parameters. The design of the QUIJOTE

simulations enables this novel approach to identify and quantify information content from new observables.

4.3. Likelihood-free inference

Besides quantifying the information content on cosmological observables, the QUIJOTE simulations have been designed to provide enough data to train machine learning algorithms. In this subsection we present a very simple application using a well-known machine learning algorithm: the random forest.

We use the 2000 standard simulations of the LH latin-hypercube run at fiducial resolution. For each simulation, we compute the 1-dimension PDF when the density

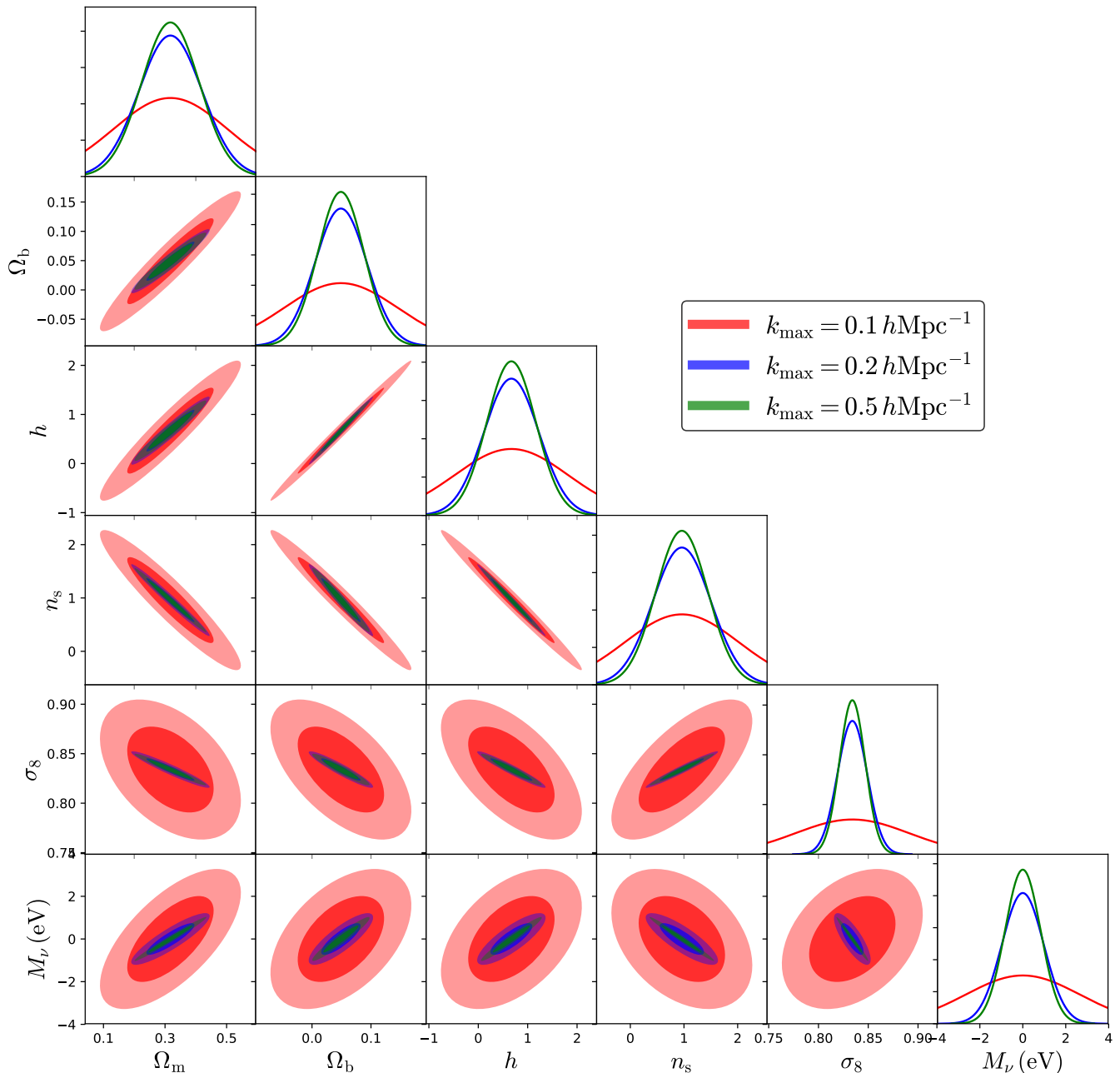


Figure 5. Constraints on the value of the cosmological parameters from the matter power spectrum in real-space at $z = 0$ for $k_{\max} = 0.2$ (red), 0.5 (blue) and 1.0 (green) $h\text{Mpc}^{-1}$. The small and big ellipses represent the 1σ and 2σ constraints, respectively. The panels with the solid lines represent the probability distribution function of each parameter. As we move to smaller scales, the constraints on the parameters improve. On the other hand, the fact that modes on small-scales are highly coupled, limit the amount of information that can be extracted from the matter power spectrum by going to smaller scales.

field is smoothed on a scale of $5 h^{-1}\text{Mpc}$ using a top-hat filter (see subsection 3.8 for further details) at $z = 0$. For each simulation we have thus an input, the value of the PDF on a set of overdensity bins, and a label, the value of the 5 cosmological parameters that we vary on those simulations: Ω_m , Ω_b , h , n_s , and σ_8 . Our purpose, is to find the function that map these two vectors, i.e.

$$\vec{\theta} = f(\text{PDF}(1 + \delta)). \quad (10)$$

The standard way to find the function f is to develop a theoretical model that outputs the PDF for a given value

of the cosmological parameters (Uhlemann et al. 2016, 2017, 2018; Gruen et al. 2018). A different approach is to identify features in the data that can be used as a link to the value of the labels. In our case, we search features on the input data using a simple random forest regressor.

We split our data into two sets: 1) a training set with the results of 1600 simulations and 2) a test set with the remaining 400 simulations. We train the random forest algorithm using the input and output of the training set. We then use the trained random forest, to predict the value of the cosmological parameters from the PDF of

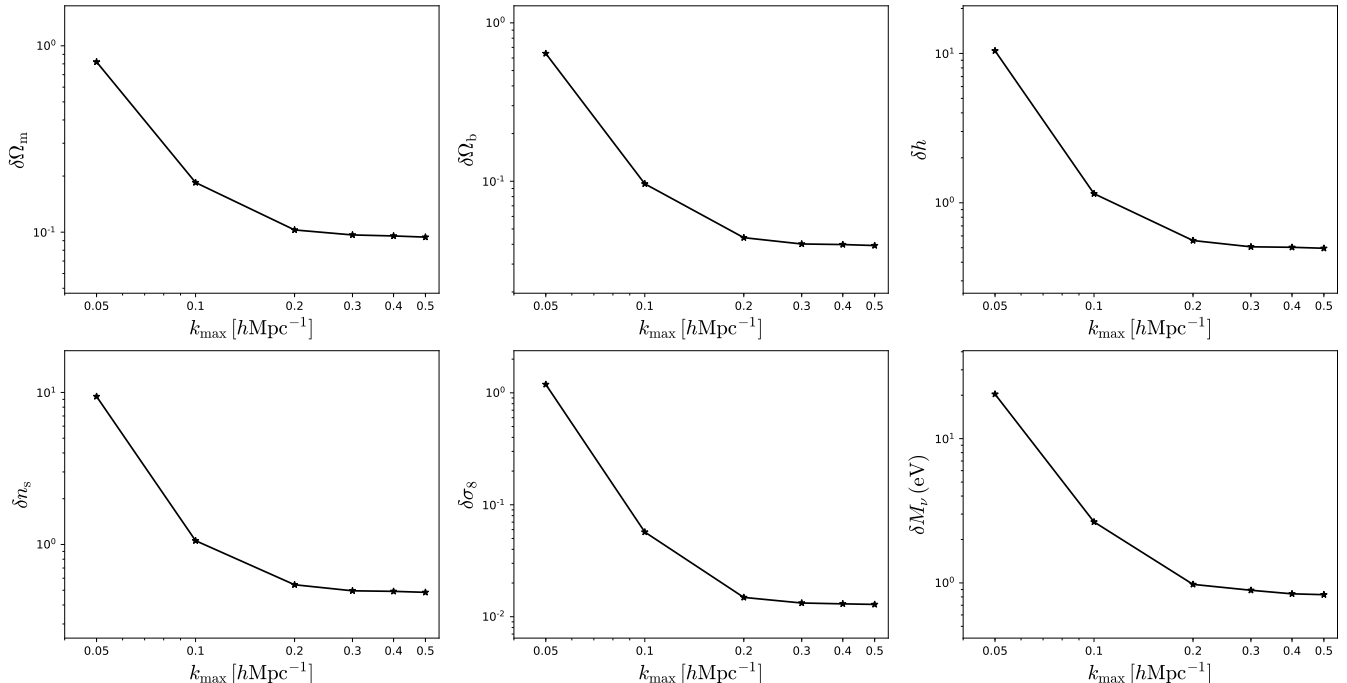


Figure 6. Marginalized 1σ constraints on the value of the cosmological parameters from the matter power spectrum in real-space at $z = 0$ as a function of k_{\max} . As we go to smaller scales, the information content on the different parameters tends to saturates. This effect is mainly driven by degeneracies among the parameters.

the simulations of the test set. We emphasize that the random forest has never seen the data from the test set, and therefore, the output from the test set is a true prediction.

We show the results on this exercise in Fig. 7. In each panel, the y-axis represents the prediction of the random forest, while the x-axis is the true value. As can be seen, the random forest learns how to accurately predict the value of σ_8 from the fully non-linear PDF without need of developing a theory model. Another parameter that the random forest is able to predict is Ω_m , although less accurately. Ω_b , h and n_s are however unconstrained by the random forest; failing to capture the parameter dependence, the random forest regressor minimizes the training loss by outputting values close to the mean of the training set. Notice that it is physically expected that for a volume of $1 (h^{-1}\text{Gpc})^3$, and only using the 1D PDF at a single smoothing scale, the constraints on those parameters will not be very tight.

It is however possible to improve these results by identifying features in the 3-dimensional density field, instead of on summary statistics. For instance, [Delgado et al. \(2019\)](#) uses convolutional neural nets to identify features that allow constraining the value of the cosmological parameter directly from the 3D density field of the QUIJOTE simulations.

4.4. New non-Gaussian statistics

In previous years, it has been shown that particular low-variance representations inspired from deep neural networks can efficiently characterize non-Gaussian fields. Based on the multi-scale decomposition achieved by the wavelet transform, these representations are built from successive applications of the so-called scattering operator on the field under study (convolution by a wavelet

followed by a modulus operator, [Mallat \(2012\)](#)), and/or from phase harmonics of its wavelet coefficients (multiplication of their phase by an integer, [Mallat et al. \(2018\)](#)). They can then be analyzed directly as well as from their covariance matrix, and have obtained state-of-the-art classification results when applied to handwritten and texture discrimination ([Bruna & Mallat 2013](#); [Sifre & Mallat 2013](#)).

The use of tailored representations to comprehensively characterize non-Gaussian fields has several advantages with respect to what can be achieved with deep neural networks. Indeed, as the structure of these representations are given and do not necessitate any training stage, they open a path to the interpretability of the results obtained ([Allys et al. 2019](#)). For the same reasons, these statistical descriptions can be used even when no large amount of data is available, since they do not need any training to be constructed. This is illustrated by the ability to synthesize very good looking synthetic fields from only one given sample, see below.

An important application of these non-Gaussian representations is to model the statistics of cosmological observations, e.g. of a projected density field. This unsupervised learning problem amounts to estimate the probability distribution of such observations, which are stationary, given one or more sample. One can then generate new maps by sampling this distribution. Following standard statistical physics approaches, the probability distribution of Quijote simulations are modeled as a maximum entropy distribution conditioned by moments [Bruna & Mallat \(2018\)](#). The main difficulty is to define appropriate moments which are sufficient to capture the statistics of the field. The right image in Fig. 8 was sampled from a Gaussian process, which is a

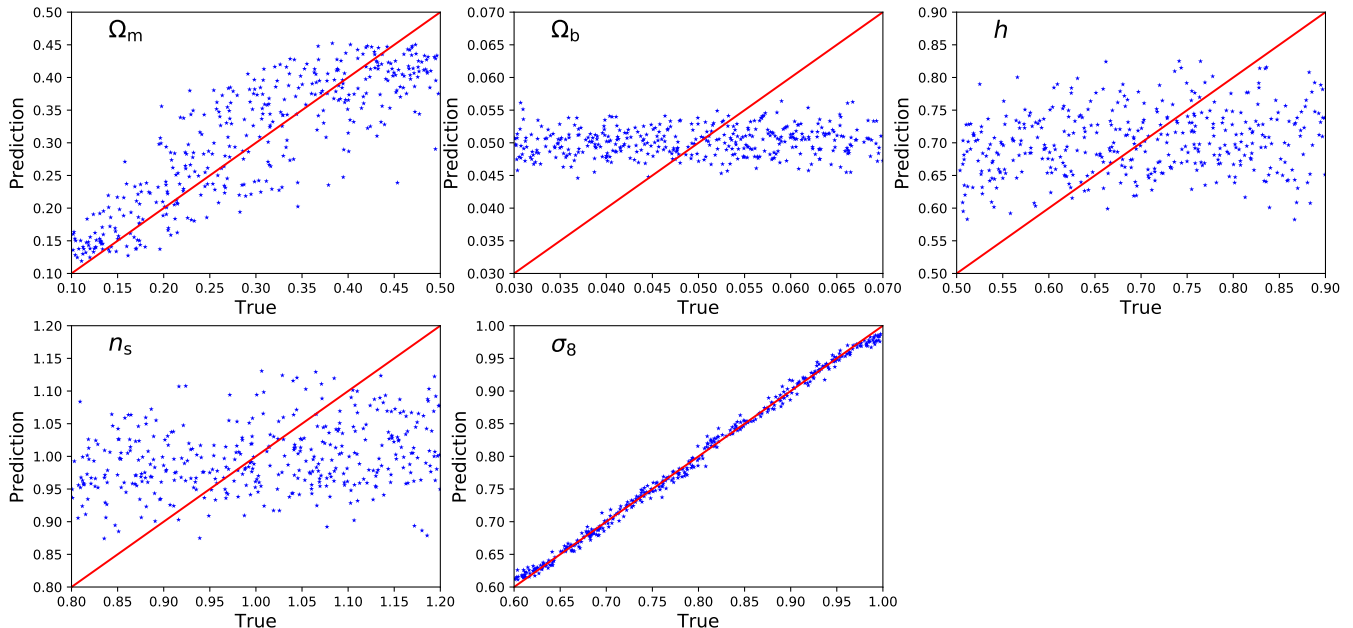


Figure 7. For each of the 2000 standard simulations at fiducial-resolution in the LH hypercube we have measured the 1-point PDF of the matter density field smoothed on a scale of $5 h^{-1}\text{Mpc}$. We have then split the data into two different sets: 1) training set (1600 simulations) and 2) test set (400 simulations). We have trained a random forest algorithm to find the mapping between the measured values of the 1-pt PDF and the value of the cosmological parameters using the training set. Once trained, we have used the test set (that the algorithm has never seen) to see how well we can predict the cosmological parameters from unlabeled PDF measurements. Each panel shows the predicted value versus the true one for Ω_m (top-left), Ω_b (top-middle), h (top-right), n_s (bottom-left), and σ_8 (bottom-middle). We find that the random forest can only predict the value of σ_8 and Ω_m from the PDF. We emphasize that no theory model/template has been used to relate the PDF with the value of the parameters.

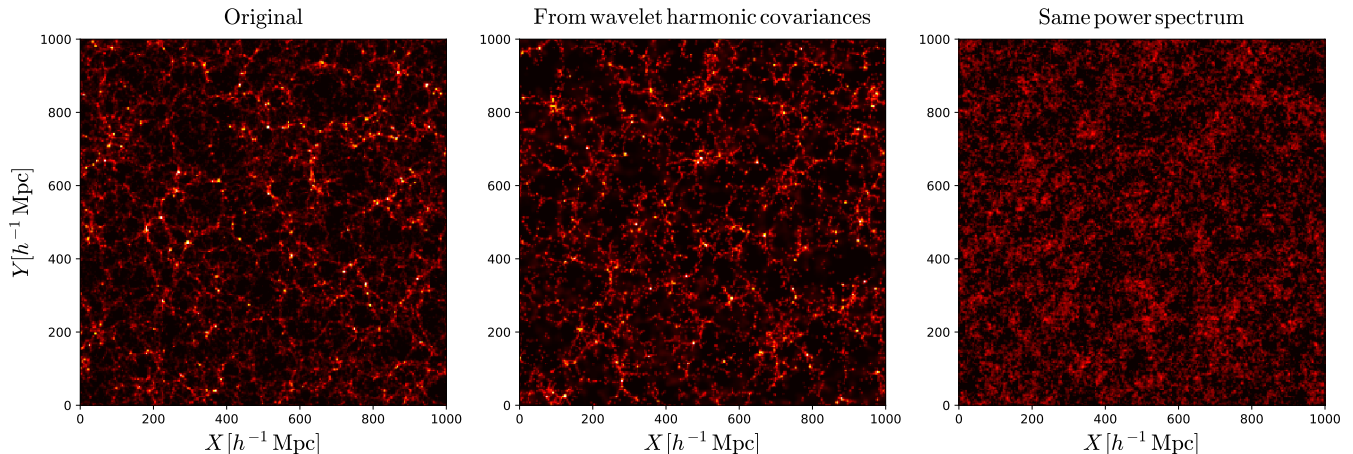


Figure 8. Left: Projected density field of a $1000 \times 1000 \times 60 (h^{-1}\text{Mpc})^3$ region at $z = 0$ for a fiducial cosmology. Center: Simulated field with the same covariance coefficients of wavelet harmonics than the original one (around one thousand coefficients). Right: Gaussian field of same power spectrum than the original one. All these images have a resolution of 256×26 pixels. One sees that in contrast to the power spectrum, the phase harmonic coefficients are efficient to extract statistical features from an image.

maximum entropy process conditioned by second order moments. It thus has the same power spectrum as the original. The middle image in Fig. 8 was sampled from a nearly maximum entropy distribution conditioned by wavelet harmonic covariance coefficients (Mallat et al. 2018). One can observe from this figure that the image obtained from wavelet harmonic covariances captures better the statistics of the original, including the geometry of high amplitude outliers and filaments, although it uses fewer moments than the Gaussian model. Indeed,

wavelet harmonic moments also depend upon the correlation of phases across scales, which are responsible for the creation of these outliers, whereas Gaussian fields have independent random phases.

A second application of these new statistical descriptors is to infer relevant physical parameters from cosmological observations, which is the goal of ongoing works. Such results would then be compared as a benchmark to the results obtained using standard statistics as e.g. the power spectrum or the bispectrum. The QUIJOTE

simulations being designed to quantify the information content on cosmological observables, they form an ideal set of data for this purpose.

4.5. Forward modeling \mathcal{E} simulation emulators

The relatively high-resolution and large parameter space of the QUIJOTE simulation suites enable us to build more accurate machine learning models of the structure formation. He et al. (2019) showed that the highly nonlinear structure formation process, simulated with particle-mesh (PM) gravity solver (Feng et al. 2016) with fixed cosmological parameters, can be emulated with convolutional neural networks (CNNs). The CNN model is trained to predict the simulation outputs given their initial conditions (linearly extrapolated to the target redshift). Its accuracy is comparable to that of the training simulations and much more than that of 2LPT commonly used to generate galaxy mocks (e.g. Scoccimarro & Sheth 2002), while at a much lower computation cost. The gain in both accuracy and efficiency proves machine learning a promising forward model of the Universe.

The QUIJOTE suite are full N -body simulations that resolve gravity to smaller scales than a PM solver. This enables training more accurate CNN models deeper into the nonlinear regime. Fig. 9 presents such an example that the machine learning model from He et al. (2019) can make accurate predictions once trained with the Quijote data.

Furthermore, with the set of latin-hypercube simulations (see Sec. 2.5), we are able to train CNN models that depend on chosen parameters in addition to the initial conditions. This allows us to build an emulator at the field level. Most of the existing emulators (e.g. Heitmann et al. 2014; Knabenhans et al. 2019; McClintock et al. 2019b; Zhai et al. 2019; McClintock et al. 2019a; Nishimichi et al. 2018; Wibking et al. 2019) are aimed mainly at predicting the ensemble averaged 2-point statistics and halo abundance. A CNN model conditional on cosmological parameters will open up the opportunity to fully exploit the information encoded in the higher-order statistics of the field.

4.6. Super-resolution simulations

Using the large quantity of high quality data available using the QUIJOTE simulations we are able to find methods with which we can accurately paint high-resolution features from computationally cheaper low-resolution simulations. The technique relies on using physically motivated networks (Kodi Ramanah et al. 2019) to perform a mapping of the distribution of the low-resolution cosmological distribution to the space of the high-resolution small scale structure. Since the information content of the high-resolution simulations is far greater than in the low-resolution simulations, we can use the information contained in the high-resolution initial conditions as a well constructed prior from which to draw the data to in-paint the small-scale structure with statistical properties that mimic those of the high-resolution training data. In Fig. 10 we show an example of the output of our network and its comparison with the high-resolution simulation.

By using this approach, not only do we obtain high-resolution simulations at a low cost, we also are able to

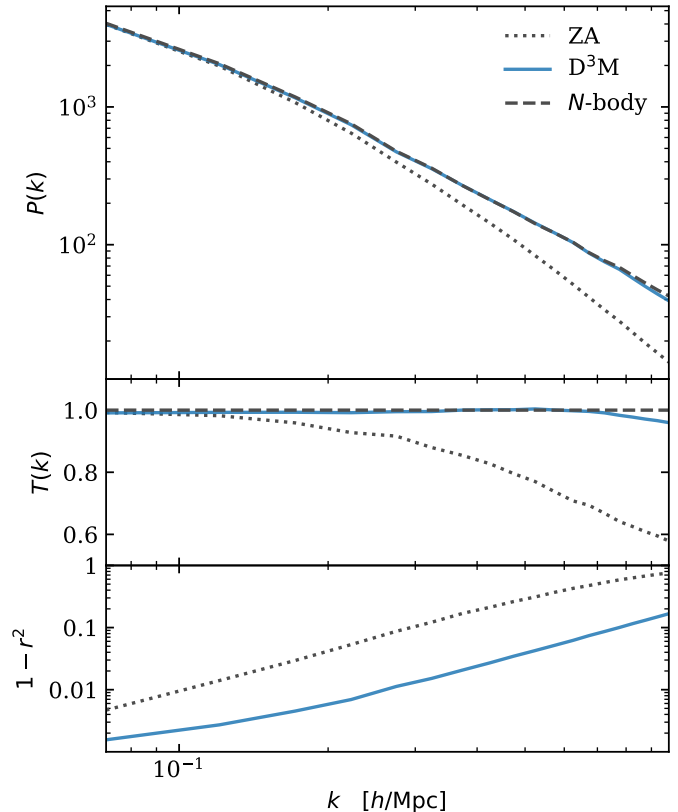


Figure 9. The top panel shows the power spectra $P(k)$ predicted by Zeldovich approximation (grey dotted), Quijote simulation (grey dashed), and CNN model dubbed D^3M (blue solid). The middle panel shows the transfer functions T – the square root of the ratio of each predicted power spectrum to that of the Quijote simulation (as the ground truth). In the bottom row we show the fraction of variance that cannot be explained by each model, by the quantity $1 - r^2$ where r is the correlation coefficient between the predicted fields and the true fields. T and r captures the quality of the model predictions. As T and r approach one, the model prediction asymptotes to the ground truth (He et al. 2019). On both benchmarks the D^3M predictions are nearly perfect from linear to nonlinear scales.

inspect the physical network to learn about how the large scale modes affect the small scale structure in real-space.

4.7. Mapping between simulations

It is possible to use machine learning algorithms to find the mapping between the positions of particles in simulations with different cosmologies. In this way, from one simulation with a given cosmology it is possible to get new simulations with different cosmologies. This can be very useful in order to densely sample the parameter space or to compute covariance matrices in different regions of the parameter space.

Giusarma & et. al (2019) use deep convolutional neural networks to establish the link between the displacement field

$$\vec{d}_k = \vec{x}_{f,k} - \vec{x}_{i,k} \quad (11)$$

where $\vec{x}_{f,k}$ and $\vec{x}_{i,k}$ are the final and initial position of particle k , in simulations with massless neutrinos and simulations with massive neutrinos (see Zennaro et al. 2019, for other methods to carry out this task). In Fig. 11 we show an example of the results for a simple sum-

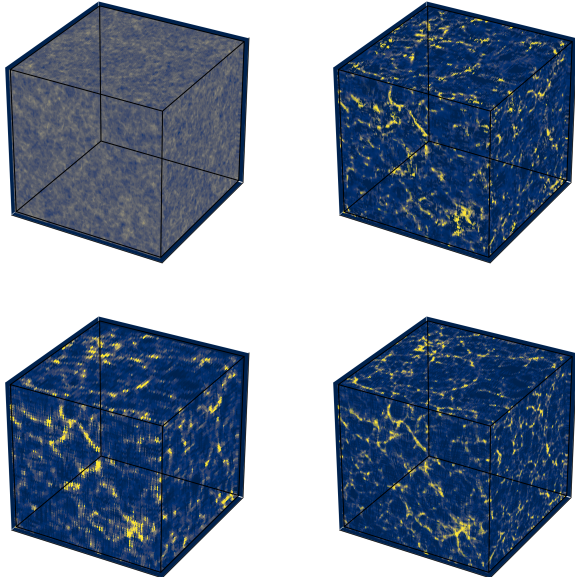


Figure 10. Example of how to increase the resolution of a simulation using deep learning. We combine the high-resolution initial conditions (top-left) with the $z = 0$ low-resolution snapshot (bottom-left) to produce a high-resolution snapshot at $z = 0$ (top-right). The high-resolution simulation at $z = 0$ is shown in the bottom-right panel for comparison.

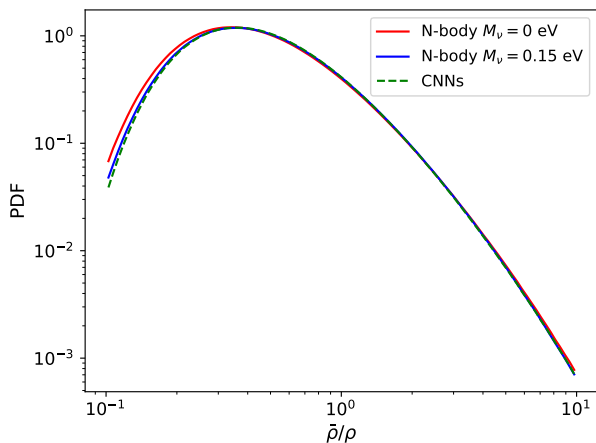


Figure 11. The red and blue lines show the probability distribution function (PDF) of the CDM+baryons field for a cosmology with massless and massive neutrinos, respectively. We train neural networks to find the mapping between the massless and massive neutrino cosmologies. The dashed green line displays the PDF of the generated CDM+baryon field from the massless neutrino density field, showing a very good agreement with the expected blue line.

mary statistics: the 1D PDF.

4.8. Statistical properties of paired fixed simulations

The large number of paired fixed simulations available in the QUIJOTE simulations allow to investigate in detail their statistical properties. These simulations can save a lot of computational resources since they have been shown to largely reduce the amplitude of cosmic variance on certain statistics. Thus, they can be used to build emulators, evaluate likelihoods...etc.

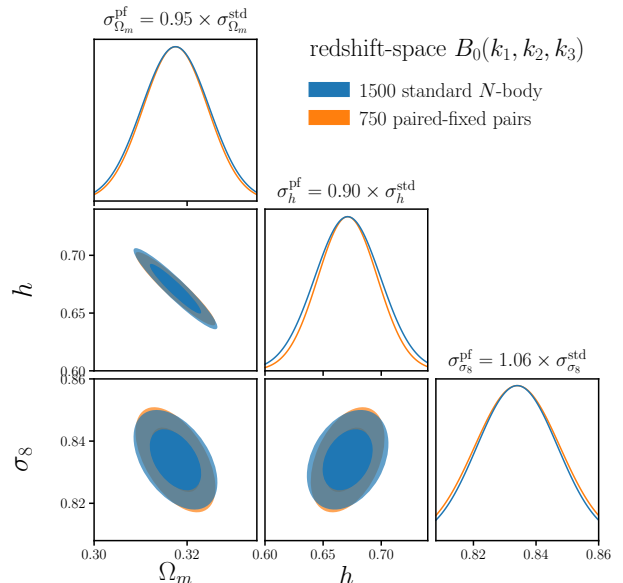


Figure 12. We use the Fisher matrix formalism to quantify how accurately the redshift-space halo bispectrum (down to $k_{\max} = 0.5 h\text{Mpc}^{-1}$) can constrain Ω_m , σ_8 and h . In blue and orange we show the results when the partial derivatives are computed using standard and paired fixed simulations. We find that results are consistent and, therefore, paired fixed simulations do not introduce a significant bias for the halo bispectrum.

Hahn & et. al (2019) studies the impact of paired fixed simulations on the halo bispectrum and performs a Fisher matrix analysis using both standard and paired fixed simulations to evaluate the derivatives. They quantify how the constraints on the cosmological parameters are affected by using standard versus paired fixed simulations to evaluate the numerical derivatives. We show some results for a subset of the parameters in Fig. 12.

5. RESOLUTION TESTS

In this section we present some tests performed on the QUIJOTE simulations to quantify the convergence of the simulations on several properties.

5.1. Zel'dovich versus 2LPT

The reason why we use the Zel'dovich approximation to generate initial conditions for cosmologies with massive neutrinos, and not 2LPT, is because, to our knowledge, it is unknown how to estimate the second-order scale-dependent growth factor and growth rate needed to use 2LPT in massive neutrino models.

Generating the initial conditions via Zel'dovich, instead of 2LPT, can induce small changes in the dynamics of the simulation particles, that can lead to small statistical differences (Crocce et al. 2006). In order to quantify this effect, we have computed the matter and the halo power spectra (for halos with masses above $3.2 \times 10^{13} h^{-1} M_\odot$) in 200 simulations of the fiducial cosmology: 100 simulations with Zeldovich ICs and 100 simulations with 2LPT ICs. The random seed are matched among the two sets. We show the results in Fig. 13.

In the top panels we show the results for the matter power spectrum in real-space (top-left) and redshift-space (top-right). We find that differences in real-space are below 1.5% at all the redshifts, while in redshift-space

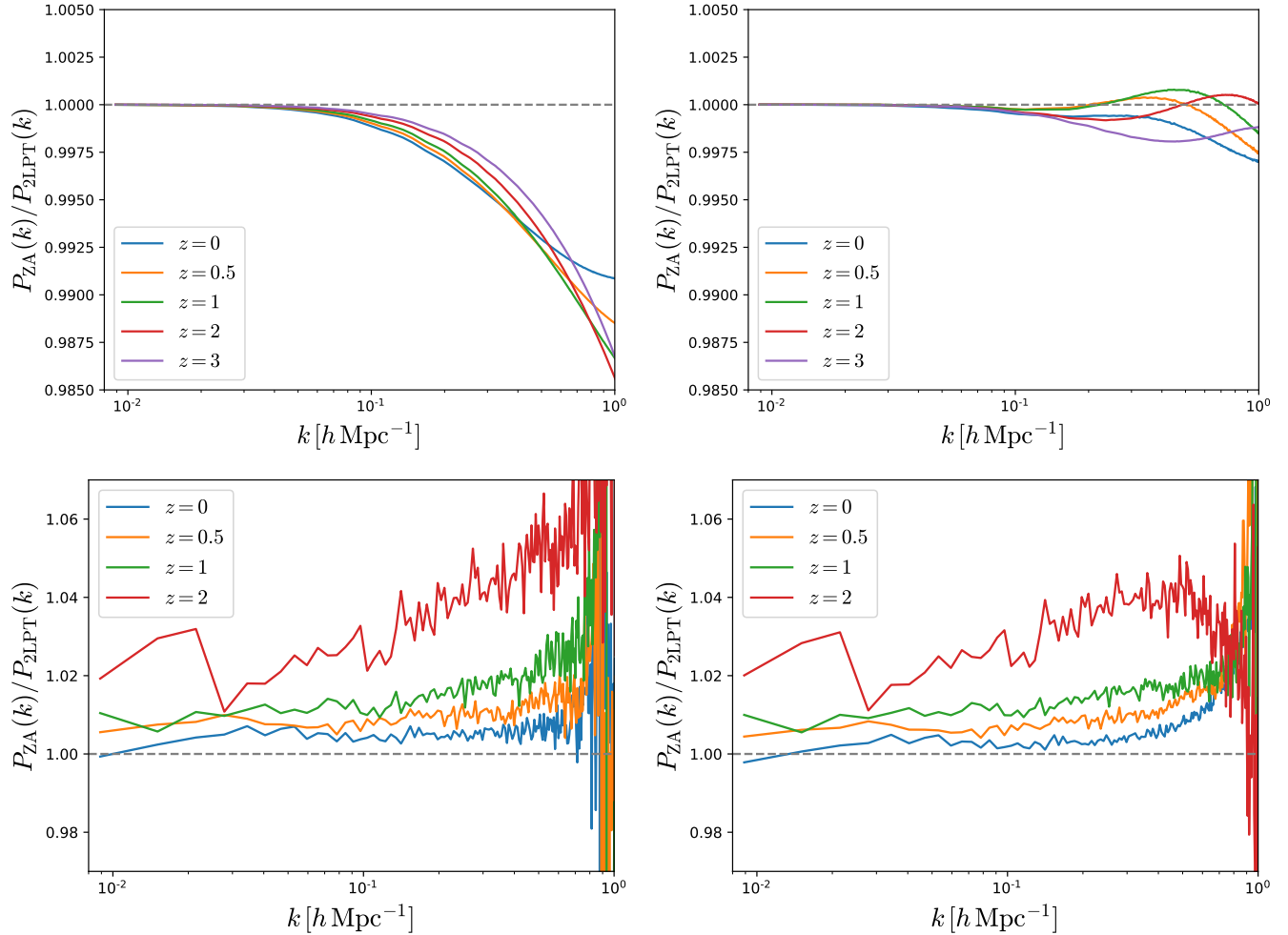


Figure 13. Effect on the matter power spectrum in real- (top-left) and redshift-space (top-right) of generating the ICs using the Zel’dovich approximation versus 2LPT. The bottom panels show the same for the power spectrum of halos with masses above $3.2 \times 10^{13} h^{-1} M_{\odot}$ in real- (bottom-left) and redshift-space (bottom-right). The plots show the ratio between the two power spectra as a function of wavenumber for different redshifts. For matter in real-space, the effect is below 1.5%, while in redshift-space the effect is below 0.5% on all scales. For halos at low-redshift, the effect is $\lesssim 1\%$. Near $k = 1 h\text{Mpc}^{-1}$, the halo power spectrum becomes negative (after subtracting shot-noise), and is severely affected by numerical noise. Since the ICs of the massive neutrino simulations have been generated using the ZA, in comparison with 2LPT for the other models, it is important to keep in mind this effect when computing numerical derivatives.

the effects are much smaller; below 0.25%. In the bottom panels we show the results for the power spectrum of halos in real-space (bottom-left) and redshift-space (bottom-right). We have corrected for Poissonian shot-noise by subtracting $1/\bar{n}$ to the measurements, where \bar{n} is the number density of halos. Results at $z = 3$ are very noisy, due to the very low number density of halos, thus, for clarity we do not show them. We find that differences in real- and redshift-space at low redshift are below $\simeq 1\%$. The higher the redshift the larger the differences. The large variations we observe around $k = 1 h\text{Mpc}^{-1}$ are due to the halos power spectrum becoming very small, and therefore highly affected by numerical noise. Notice that at low-redshift, most of the differences we observe between the halos power spectra have a very mild scale-dependence. Thus, marginalizing over an overall amplitude can get rid of most of this effect.

We also carry out the above analysis for the bispectrum of halos in real- and redshift-space at $z = 0$ down to

$k_{\text{max}} = 0.5 h\text{Mpc}^{-1}$. We find that differences in redshift-space can be around 10%, and slightly larger in real-space.

When making Fisher forecasts analysis, it is important to keep this effect in mind, as the additional scale-dependent present in the models with massive neutrinos may slightly affect the results. For this reason, when computing derivatives with respect to neutrino masses, we recommend using the simulations with Zel’dovich initial conditions from the fiducial model, instead of the 2LPT ones.

5.2. Clustering

One important aspect to consider when analyzing numerical simulations is the range of scales where results are converged. In order to quantify this, we have used three simulations, all within the fiducial cosmology, but run at different resolutions: high-resolution (1024^3 particles), fiducial-resolution (512^3 particles), and low-resolution (256^3 particles).

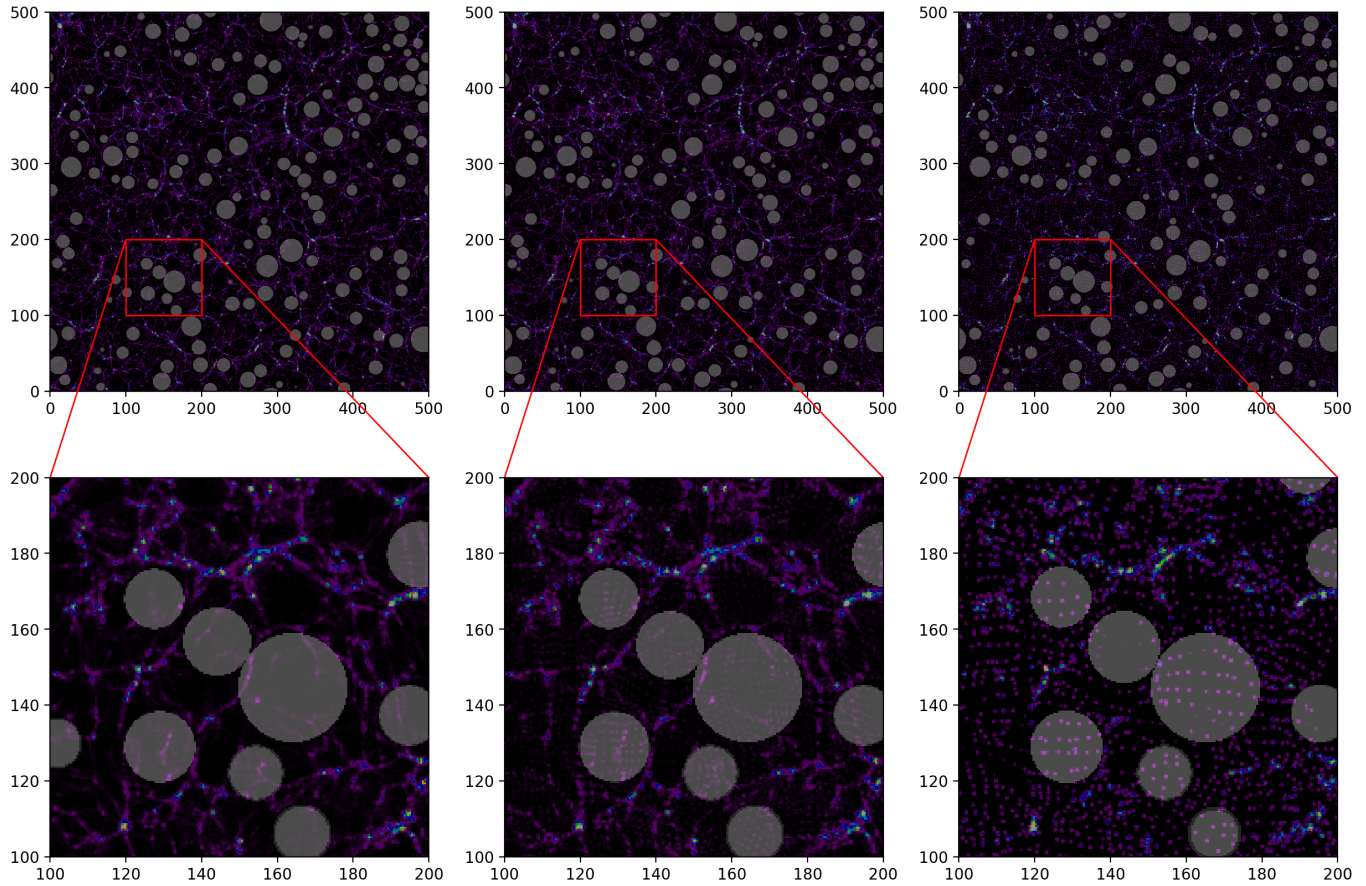


Figure 14. We have identified voids (white spheres) in three simulations with the same random seed but different mass and spatial resolutions at $z = 0$. As can be seen, our void finder is relatively robust against these changes, at least for the largest voids.

In Fig. 14 we show the projected matter overdensity field in a slice of $500 \times 500 \times 10 (h^{-1}\text{Mpc})^3$ for the three different simulations. As the amplitudes and phases of the modes that are common across the simulations are the same, the large-scale density field in the three images is basically the same. Differences show up on small scales, where different modes across simulations are present/absent. Resolution effects are clearly visible in the image: while in the low-resolution simulation we can see individual particles in cosmic voids, in the high-resolution the density field is much smoother.

We have computed the matter power spectrum for those three simulations at redshifts 0, 0.5, 1, 2, and 3. We show the results in Fig. 15. We find that at $z = 0$, the results of the fiducial-resolution run are converged all the way to $k = 1 h\text{Mpc}^{-1}$ at 2.5%. At higher redshifts, the results are only converged on larger scales; e.g. at $z = 3$, only scales $k \simeq 0.4 h\text{Mpc}^{-1}$ are converged at the fiducial-resolution. We note that although the relative small scales error increases with redshift on, the absolute error do decrease, since the amplitude of the power spectrum shrinks with redshift.

We emphasize that these tests indicate the range of scales where the absolute amplitude of the clustering should be trusted within a given accuracy. Numerical derivatives of statistics with respect to cosmological parameters may be converged to smaller scales, since it is expected that relative differences propagate among mod-

els, and taking differences cancel out them.

5.3. Void finder

The void finder (see subsection 3.3) we have run on the QUIJOTE simulations has some nice properties. One of them, is that the positions and sizes of cosmic voids are not largely affected by the mass and spatial resolution of the simulation¹⁴.

In Fig. 14 we show the location and sizes of voids identified in 3 different simulations with the same random seed but different mass and spatial resolutions. As can be seen, the locations and sizes of voids among simulations are very similar, pointing out the robustness of our void finder against mass and spatial resolution.

6. SUMMARY

In this paper we have introduced the QUIJOTE simulations, a large set of 43100 full N-body simulations spanning thousands of different cosmologies and containing, at a single redshift, more than 8.5 trillion (8.5×10^{12}) particles. Billions of dark matter halos and cosmic voids have been identified in the simulations, that required more than 35 million CPU hours to be run.

The QUIJOTE simulations have been designed to accomplish two main goals

¹⁴ We are of course assuming that the sizes of the voids are larger than the spatial resolution of the density field.

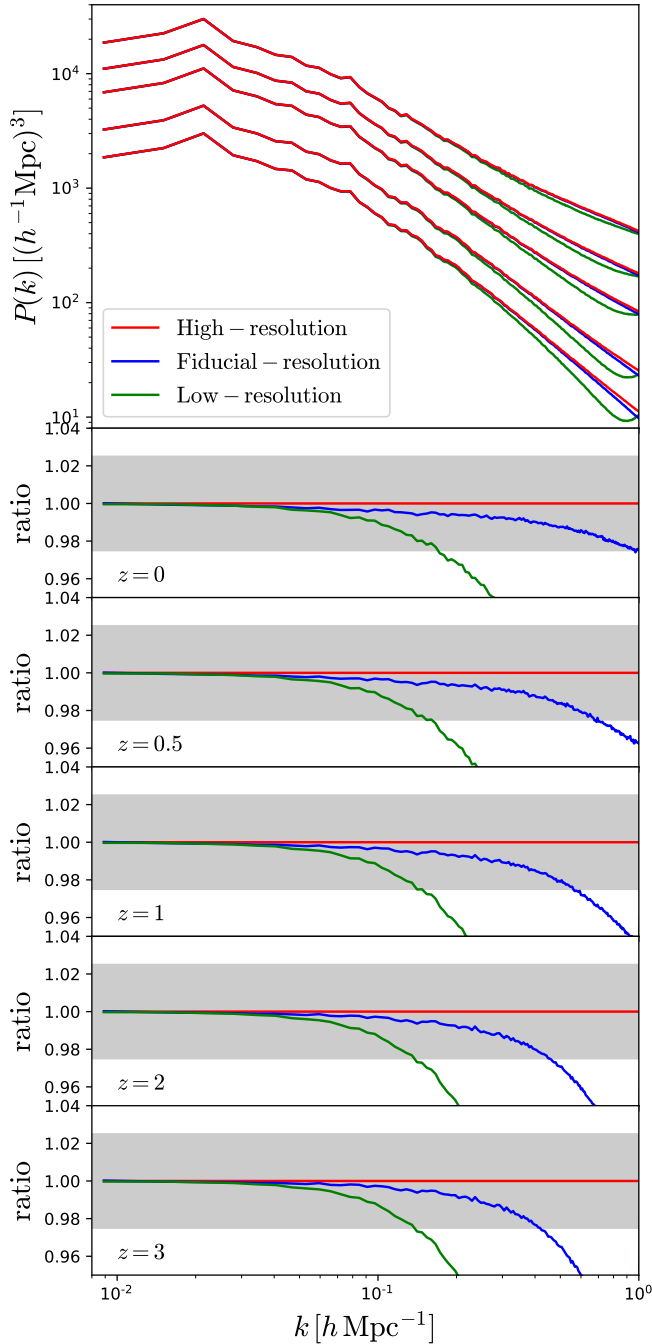


Figure 15. Matter power spectrum for a realization of the fiducial cosmology run at three different resolutions: 1) high-resolution (red lines), 2) fiducial-resolution (blue lines), and 3) low-resolution (green lines). The upper panel shows the different power spectra from $z = 0$ (top-lines) to $z = 3$ (bottom lines). The small panels display the ratio between the different power spectra at different redshifts. At $z = 0$, the matter power spectrum is converged all the way to $k = 1 h\text{Mpc}^{-1}$ at 2.5%, while at $z = 3$ this scale shrinks to $k \simeq 0.4 h\text{Mpc}^{-1}$.

- Quantify the information content on cosmological observables
- Provide enough statistics to train machine learning algorithms

It is clear that there are many possible uses for these simulations beyond the ones we have mentioned in here (see e.g. [Obuljen et al. 2019](#)). We make the data from the QUIJOTE simulations freely available to the community with the goal to allow the broadest possible exploration of their applications.

We believe the QUIJOTE simulations will complement very well the large efforts carried out by the community (see e.g. [DeRose et al. 2019](#); [Nishimichi et al. 2018](#); [Heitmann et al. 2014](#); [Knabenhans et al. 2019](#); [Garrison et al. 2018](#)).

Instructions on how to download the data can be found in <https://github.com/franciscovillaescusa/Quijote-simulations>. As far as our storage resources allow, we will distribute all data products: e.g. halo and void catalogues, power spectra, marked power spectra, correlation functions, bispectra, PDFs, and full snapshots. The total data generated by the QUIJOTE simulations exceeds 1 Petabyte.

We also provide a set of python libraries, PYLIANS, developed for many years, to help with the analysis of the data. PYLIANS can be found in <https://github.com/franciscovillaescusa/Pylians>.

ACKNOWLEDGEMENTS

We are specially thankful to Nick Carriero and Dylan Simon from the Flatiron Institute, and Mahidhar Tatineni from the San Diego Supercomputer Center for their immense help with the multiple technical problems we have faced while running the simulations. We thank Volker Springel for giving us access to Gadget-III. The work of SH, EG, EM, DS, FVN, and BDW is supported by the Simons Foundation. CDK acknowledges the support of the National Science Foundation award number DGE1656466 at Princeton University. AP is supported by NASA grant 15-WFIRST15-0008 to the WFIRST Science Investigation Team ‘‘Cosmology with the High Latitude Survey’’. LV acknowledges support from the European Union Horizon 2020 research and innovation program ERC (BePreSySe, grant agreement 725327) and MDM-2014-0369 of ICCUB (Unidad de Excelencia Maria de Maeztu. BDW also acknowledges financial support from ANR BIG4 project, under reference ANR-16-CE23-0002. AMD acknowledges support from AstroCom NYC, NSF award AST-1831412 and Simons Foundation award number 533845. SH thanks NASA for their support in grant number: NASA grant 15-WFIRST15-0008 and NASA Research Opportunities in Space and Earth Sciences grant 12-EUCLID12-0004.

REFERENCES

- Allys, E., Levrier, F., Zhang, S., Colling, C., Blancard, B., Boulanger, F., Hennebelle, P., & Mallat, S. 2019, arXiv preprint arXiv:1905.01372
- Alsing, J., Charnock, T., Feeney, S., & Wandelt, B. 2019, MNRAS, 488, 4440, [arXiv:1903.00007]
- Alsing, J., & Wandelt, B. 2018, MNRAS, 476, L60, [arXiv:1712.00012]

- Anderson, L., Pontzen, A., Font-Ribera, A., Villaescusa-Navarro, F., Rogers, K. K., & Genel, S. 2018, arXiv e-prints, arXiv:1811.00043, [arXiv:1811.00043]
- Angulo, R. E., & Pontzen, A. 2016, *MNRAS*, 462, L1, [arXiv:1603.05253]
- Armijo, J., Cai, Y.-C., Padilla, N., Li, B., & Peacock, J. A. 2018, *Mon. Not. Roy. Astron. Soc.*, 478, 3627, [arXiv:1801.08975]
- Banerjee, A., & Dalal, N. 2016, *J. Cosmology Astropart. Phys.*, 2016, 015, [arXiv:1606.06167]
- Banerjee, A., Powell, D., Abel, T., & Villaescusa-Navarro, F. 2018, *J. Cosmology Astropart. Phys.*, 2018, 028, [arXiv:1801.03906]
- Beisbart, C., & Kerscher, M. 2000, *Astrophys. J.*, 545, 6, [arXiv:astro-ph/0003358]
- Blot, L., Corasaniti, P. S., Alimi, J.-M., Reverdy, V., & Rasera, Y. 2015, *MNRAS*, 446, 1756, [arXiv:1406.2713]
- Blot, L., Corasaniti, P. S., Amendola, L., & Kitcing, T. D. 2016, *MNRAS*, 458, 4462, [arXiv:1512.05383]
- Brandbyge, J., Hannestad, S., Haugbølle, T., & Thomsen, B. 2008, *J. Cosmology Astropart. Phys.*, 8, 20, [arXiv:0802.3700]
- Bruna, J., & Mallat, S. 2013, *IEEE transactions on pattern analysis and machine intelligence*, 35, 1872
- . 2018, arXiv preprint arXiv:1801.02013
- Carron, J. 2013, *A&A*, 551, A88, [arXiv:1204.4724]
- Charnock, T., Lavaux, G., & Wandelt, B. D. 2018, *Phys. Rev. D*, 97, 083004, [arXiv:1802.03537]
- Chuang, C.-H. et al. 2019, *MNRAS*, 487, 48, [arXiv:1811.02111]
- Crocce, M., Pueblas, S., & Scoccimarro, R. 2006, *MNRAS*, 373, 369, [arXiv:astro-ph/0606505]
- Davis, M., Efstathiou, G., Frenk, C. S., & White, S. D. M. 1985, *ApJ*, 292, 371
- Delgado, A. M., Villaescusa-Navarro, F., & et. al. 2019
- DeRose, J. et al. 2019, *ApJ*, 875, 69, [arXiv:1804.05865]
- Feng, Y., Chu, M.-Y., & Seljak, U. 2016, arXiv e-prints, [arXiv:1603.00476]
- Garrison, L. H., Eisenstein, D. J., Ferrer, D., Tinker, J. L., Pinto, P. A., & Weinberg, D. H. 2018, *Astrophys. J. Suppl.*, 236, 43, [arXiv:1712.05768]
- Giusarma, E., & et. al. 2019
- Gottloeber, S., Kerscher, M., Kravtsov, A. V., Faltenbacher, A., Klypin, A., & Mueller, V. 2002, *Astron. Astrophys.*, 387, 778, [arXiv:astro-ph/0203148]
- Gruen, D. et al. 2018, *Physical Review D*, 98, 023507, [arXiv:1710.05045]
- Hahn, C., & et. al. 2019
- Hahn, C., Villaescusa-Navarro, F., Castorina, E., & Scoccimarro, R. 2019
- He, S., Li, Y., Feng, Y., Ho, S., Ravanbakhsh, S., Chen, W., & Poczós, B. 2019, *Proceedings of the National Academy of Science*, 116, 13825, [arXiv:1811.06533]
- Heitmann, K., Lawrence, E., Kwan, J., Habib, S., & Higdon, D. 2014, *ApJ*, 780, 111, [arXiv:1304.7849]
- Hernández-Aguayo, C., Baugh, C. M., & Li, B. 2018, *Mon. Not. Roy. Astron. Soc.*, 479, 4824, [arXiv:1801.08880]
- Ichiki, K., & Takada, M. 2012, *Phys. Rev. D*, 85, 063521, [arXiv:1108.4688]
- Klypin, A., Prada, F., & Byun, J. 2019, arXiv e-prints, arXiv:1903.08518, [arXiv:1903.08518]
- Knabenhans, M., et al. 2019, *Mon. Not. Roy. Astron. Soc.*, 484, 5509, [arXiv:1809.04695]
- Knollmann, S. R., & Knebe, A. 2009, *ApJS*, 182, 608, [arXiv:0904.3662]
- Kodi Ramanah, D., Charnock, T., & Lavaux, G. 2019, *Phys. Rev. D*, 100, 043515, [arXiv:1903.10524]
- Kodwani, D., Alonso, D., & Ferreira, P. 2019, *The Open Journal of Astrophysics*, 2, 3, [arXiv:1811.11584]
- Leclercq, F., Pisani, A., & Wandelt, B. D. 2014, arXiv e-prints, arXiv:1403.1260, [arXiv:1403.1260]
- Lewis, A., Challinor, A., & Lasenby, A. 2000, *ApJ*, 538, 473, [arXiv:astro-ph/9911177]
- LoVerde, M., & Zaldarriaga, M. 2014, *Phys. Rev. D*, 89, 063502, [arXiv:1310.6459]
- Mallat, S. 2012, *Communications on Pure and Applied Mathematics*, 65, 1331
- Mallat, S., Zhang, S., & Rochette, G. 2018, arXiv preprint arXiv:1810.12136
- Massara, E., Villaescusa-Navarro, F., & et al. 2019
- McClintock, T. et al. 2019a, [arXiv:1907.13167]
- . 2019b, *Astrophys. J.*, 872, 53, [arXiv:1804.05866]
- Nishimichi, T. et al. 2018, arXiv e-prints, arXiv:1811.09504, [arXiv:1811.09504]
- Obuljen, A., Dalal, N., & Percival, W. J. 2019, arXiv e-prints, arXiv:1906.11823, [arXiv:1906.11823]
- Perlmutter, S. et al. 1999, *ApJ*, 517, 565, [arXiv:astro-ph/9812133]
- Planck Collaboration et al. 2018, arXiv e-prints, arXiv:1807.06209, [arXiv:1807.06209]
- . 2019, arXiv e-prints, arXiv:1905.05697, [arXiv:1905.05697]
- Pontzen, A., Slosar, A., Roth, N., & Peiris, H. V. 2016, *Phys. Rev. D*, 93, 103519, [arXiv:1511.04090]
- Ravanbakhsh, S., Oliva, J., Fromenteau, S., Price, L. C., Ho, S., Schneider, J., & Poczós, B. 2017, arXiv e-prints, arXiv:1711.02033, [arXiv:1711.02033]
- Riess, A. G. et al. 1998, *AJ*, 116, 1009, [arXiv:astro-ph/9805201]
- Scoccimarro, R. 2015, *Physical Review D*, 92, [arXiv:1506.02729]
- Scoccimarro, R., & Sheth, R. K. 2002, *MNRAS*, 329, 629, [arXiv:astro-ph/0106120]
- Sefusatti, E., Crocce, M., Scoccimarro, R., & Couchman, H. M. P. 2016, *Monthly Notices of the Royal Astronomical Society*, 460, 3624
- Sefusatti, E., & Scoccimarro, R. 2005, *Physical Review D*, 71, [arXiv:astro-ph/0412626]
- Sheth, R. K., Connolly, A. J., & Skibba, R. 2005, Submitted to: *Mon. Not. Roy. Astron. Soc.*, [arXiv:astro-ph/0511773]
- Sifre, L., & Mallat, S. 2013, in *Proceedings of the IEEE conference on computer vision and pattern recognition*, 1233–1240
- Springel, V. 2005, *MNRAS*, 364, 1105, [arXiv:arXiv:astro-ph/0505010]
- Tegmark, M., Taylor, A. N., & Heavens, A. F. 1997, *ApJ*, 480, 22, [arXiv:astro-ph/9603021]
- Uhlemann, C., Codis, S., Kim, J., Pichon, C., Bernardeau, F., Pogosyan, D., Park, C., & L’Huillier, B. 2017, *Monthly Notices of the Royal Astronomical Society*, 466, 2067, [arXiv:1607.01026]
- Uhlemann, C., Codis, S., Pichon, C., Bernardeau, F., & Reimberg, P. 2016, *Monthly Notices of the Royal Astronomical Society*, 460, 1529, [arXiv:1512.05793]
- Uhlemann, C. et al. 2018, *Monthly Notices of the Royal Astronomical Society*, 473, 5098, [arXiv:1705.08901]
- Valogiannis, G., & Bean, R. 2018, *Phys. Rev.*, D97, 023535, [arXiv:1708.05652]
- Verde, L. 2007, arXiv e-prints, arXiv:0712.3028, [arXiv:0712.3028]
- Viel, M., Haehnelt, M. G., & Springel, V. 2010, *J. Cosmology Astropart. Phys.*, 6, 015, [arXiv:1003.2422]
- Villaescusa-Navarro, F., Bird, S., Peña-Garay, C., & Viel, M. 2013, *J. Cosmology Astropart. Phys.*, 3, 019, [arXiv:1212.4855]
- Villaescusa-Navarro, F., Massara, E., & et al. 2019
- Villaescusa-Navarro, F., Miralda-Escudé, J., Peña-Garay, C., & Quilis, V. 2011, *J. Cosmology Astropart. Phys.*, 6, 027, [arXiv:1104.4770]
- Villaescusa-Navarro, F. et al. 2018, *ApJ*, 867, 137, [arXiv:1806.01871]
- Wandelt, B. D. 2013, in *Astrostatistical Challenges for the New Astronomy*, 1013
- White, M. 2016, *JCAP*, 1611, 057, [arXiv:1609.08632]
- Wibking, B. D. et al. 2019, *Mon. Not. Roy. Astron. Soc.*, 484, 989, [arXiv:1709.07099]
- Zel’dovich, Y. B. 1970, *A&A*, 5, 84
- Zennaro, M., Angulo, R. E., Aricò, G., Contreras, S., & Pellejero-Ibáñez, M. 2019, arXiv e-prints, arXiv:1905.08696, [arXiv:1905.08696]
- Zennaro, M., Bel, J., Villaescusa-Navarro, F., Carbone, C., Sefusatti, E., & Guzzo, L. 2017, *MNRAS*, 466, 3244, [arXiv:1605.05283]
- Zhai, Z. et al. 2019, *Astrophys. J.*, 874, 95, [arXiv:1804.05867]